EUROPEAN ORGANIZATION FOR NUCLEAR RESEARCH

Measurements of Single Diffraction at $\sqrt{s} = 630$ GeV; Evidence for a Non-Linear $\alpha(t)$ of the $\mathcal{P}$omeron

A. Brandt[1], S. Erhan[a], A. Kuzucu[2], D. Lynn[3], M. Medinnis[4],
N. Ozdes[2], P.E. Schlein[b] M.T. Zeyrek[5], J.G. Zweizig[6]
University of California*, Los Angeles, California 90095, USA.

J.B. Cheze, J. Zsembery
Centre d'Etudes Nucleaires-Saclay, 91191 Gif-sur-Yvette, France.

(UA8 Collaboration)

Abstract

We report measurements of the inclusive differential cross section for the single-diffractive reactions: $p_i + \bar{p} \to p_f + X$ and $p + \bar{p}_i \to X + \bar{p}_f$ at $\sqrt{s} = 630$ GeV, in the momentum transfer range, $0.8 < -t < 2.0$ GeV^2 and final state Feynman-$x_p > 0.90$. Based on the assumption of factorization, several new features of the $\mathcal{P}$omeron Flux Factor are determined from simultaneous fits to our UA8 data and lower energy data from the CHLM collaboration at the CERN-Intersecting Storage Rings.

Prominent among these is that the effective $\mathcal{P}$omeron Regge trajectory requires a term quadratic in t, with coefficient, $\alpha'' = 0.079 \pm 0.012$ GeV^{-4}. We also show that the data require a $\mathcal{P}$omeron-proton cross section that first decreases with increasing diffractive mass (corresponding to the $\mathcal{PPR}$ term in the triple-Regge expansion) and then increases at larger mass (the $\mathcal{PPP}$ term), similar to real particle total cross sections. We measure the product, $K\sigma_0 = 0.72 \pm 0.10$ mb GeV^{-2}, where K is the normalization constant of the $\mathcal{P}$omeron Flux Factor in the proton and σ_0 is the scale constant in the $\mathcal{P}$omeron-proton total cross section. Finally, we report the occurence of "beam jets" in the $\mathcal{P}$omeron direction in the rest frame of the diffractive system.

Contents

1 Introduction

We report a study of the single-diffractive reaction:

$$p_i + \bar{p} \rightarrow p_f + X \tag{1}$$

and its charge conjugate at the CERN S$p\bar{p}$S-Collider with $\sqrt{s} = 630$ GeV, where p_i and p_f are, respectively, the inital and final state proton momenta.

One of the most remarkable phenomena in strong interaction physics occurs in reactions of this type, which have beam-like particles in the final state. It has been known for many years[1] that the inclusive spectra of final-state particles which have the identity of the beam particle increase rapidly as Feynman-x of the particle approachs unity, in striking contrast with the $(1\text{-}x)^n$ (with $n > 0$) type of falling spectra observed for all other particle types. Figure 1 shows such a spectrum for final state antiprotons[1] in the charge conjugate of React. 1. For $x_p < 0.97$, the distribution is rather flat but with a much larger cross section than for other baryons. For example, this is shown in Fig. 2 for many types of final-state baryons[2, 3]. The exponent which labels each data set in the figure depends inversely on the number of beam valence quarks in the final-state baryon; thus, the relatively flat proton distribution is consistent with the expectation that the final-state proton contains all the valence quarks of the beam proton.

In React. 1, an observed rapidity gap between p_f and X in the final state signifies that the entire residual momentum of the proton (with beam fraction, $\xi = 1 - x_p$) participates in the interaction between it and the second beam particle. This effect has been described[1] in terms of an exchange of the $\mathcal{P}$omeron Regge trajectory, which embodies the idea of "factorization". The interacting vectors of the $p\bar{p}$ system shown in Fig. 3(a) can be rearranged in the so-called "t-channel exchange diagram" shown in part (b) of the figure. The exchanged entity, with beam momentum fraction, $\xi = 1 - x_p$, and squared-momentum-transfer[2], $t = (p_i - p_f)^2$, is the $\mathcal{P}$omeron. The upper vertex is a collision with center-of-mass energy $\sqrt{s'}$, between the $\bar{p}$ and the soft $\mathcal{P}$omeron-dominated component of p_i.

Since $x_p \sim 1$ is the most likely beam momentum fraction of the final state p_f or $\bar{p}_f$, correspondingly the most likely value of the $\mathcal{P}$omeron's momentum fraction, ξ, is near zero[3]. Thus, a proton beam is essentially a beam of low momentum $\mathcal{P}$omerons, as depicted in Fig. 3(a). To good approximation, the invariant squared-mass of the X-system, s', is kinematically related to the total squared-energy in the initial state, s, by the relation: $s' = \xi s$. Thus, a measurement of x_p tags diffractive events with diffractive mass, $\sqrt{s'}$. In high energy collisions, s' can be quite large. For example, in the experiment reported here, when $x_p = 0.95$ (0.90), we have $\sqrt{s'} = 140$ (200) GeV.

The concept of factorization and the possibility to transfer large amounts of energy-momentum at high energy led Ingelman and Schlein[4] to propose that, in React. 1 (and, analogously, also in (virtual) γp interactions in ep scattering), it should be possible to

---

[1]Since we henceforth discuss protons (antiprotons), we use the notation, x_p.

[2]We use the metric where t is negative in the physical region

[3]Because $x_p + \xi = 1$, these are equivalent variables, and we use them interchangably in this paper.

observe hard scattering in the $\mathcal{P}$omeron-proton interaction and to obtain information about the partonic structure of the $\mathcal{P}$omeron.

Finding and studying jet production in React. 1 was the original purpose of this experiment and positive results were reported in three previous UA8 papers[5, 6, 7]. Jets were observed[5] which possessed typical QCD properties, thus establishing that the $\mathcal{P}$omeron has a partonic structure. Subsequent UA8 jet results[6] on React. 1 from the 1988–1989 S$p\bar{p}$S-Collider runs showed that the $\mathcal{P}$omeron's structure was hard, and that there appeared to be a δ-function-like component (in about 30% of the observed events), in which the entire momentum of the $\mathcal{P}$omeron enters into the hard scattering. The ZEUS[8] and H1[9] e^+p experiments at HERA and the CDF[10] and DØ [11] $p\bar{p}$ experiments at Fermilab have since reported other hard scattering results in diffraction, and "hard diffractive scattering" is now a well-established component of most high energy experiments.

These hard scattering results, together with the success of Donnachie and Landshoff[12] in using factorization and a $\mathcal{P}$omeron-photon analogy to predict React. 1 from elastic scattering measurements, give impetus to the idea that the $\mathcal{P}$omeron behaves like a *quasi-real* object inside the proton with an effective $\mathcal{P}$omeron flux factor.

Assuming the validity of factorization, the differential cross section for React. 1 can be expressed as a product of the flux factor and a $\mathcal{P}$omeron-proton scattering cross section, $\sigma_{\mathcal{P}p}^{total}$:

$$\frac{d^2\sigma}{d\xi dt} \;=\; F_{\mathcal{P}/p}(t,\xi) \;\cdot\; \sigma_{\mathcal{P}p}^{total}(s'). \tag{2}$$

In React. 1, where $\sigma_{\mathcal{P}p}^{total}$ depends relatively weakly on s', the shape of the observed $x_p = 1 - \xi$ distribution, before resolution smearing, is dominated (at low $|t|$) by a $\sim \xi^{-1}$ factor in $F_{\mathcal{P}/p}(t,\xi)$, as discussed in Sect. 5.4. Contrast this with jet production in React. 1, where $\sigma_{\mathcal{P}p}^{jets}$ is zero at low s' and rises dramatically with increasing s', such that the $x_p \sim 1$ peak is no longer visible[7, 4].

In the present paper, we present a detailed study of inclusive diffraction in React. 1. The momentum transfer is in the range $0.8 < -t < 2.0$ GeV^2 for protons and antiprotons with $x_p > 0.9$. As discussed in the following section, the final state p_f or $\bar{p}_f$ is detected in one of four Roman-pot spectrometers[13], while much of the diffractive system, X, is detected in the calorimeters of the UA2 experiment[14], installed in the same interaction region.

In Chapt. 2, the UA8 apparatus and triggers[13] are described. We describe the event selection and various corrections applied to the raw data in Chapt. 3. The resulting absolute cross sections for React. 1 are given in Chapt. 4.

A combined analysis of the UA8 data and the extensive data on React. 1 by the CHLM collaboration at the CERN Intersecting Storage Rings[15] is given in Chapt. 5. Prominent among these results is that the effective $\mathcal{P}$omeron Regge trajectory requires a term quadratic in t, with coefficient, $\alpha'' = 0.079 \pm 0.012$ GeV^{-4}. We also show that the data require a $\mathcal{P}$omeron-proton cross section that first decreases with increasing diffractive mass (corresponding to the $\mathcal{PPR}$ term in the triple-Regge expansion) and then increases

at larger mass (the $\mathcal{PPP}$ term), similar to real particle total cross sections. We measure the product, $K\sigma_0 = 0.72 \pm 0.10$ mb/GeV^2, where K is the normalization constant of the $\mathcal{P}$omeron flux factor, $F_{\mathcal{P}/p}(t,\xi)$, in the proton and σ_0 is the scale constant in the $\mathcal{P}$omeron-proton total cross section, $\sigma_{\mathcal{P}p}^{total}$. We also show that the data are consistent with a constant (s-independent) K.

Longitudinal event structure and energy-flow measurements for React. 1 are given in Chapt. 6. Pronounced "beam jets" are seen in this energy flow in the $\mathcal{P}$omeron hemisphere, where there is almost complete acceptance.

2 Apparatus

A detailed description of the UA8 apparatus, its properties, triggering capabilities and interface to the UA2 experiment are given elsewhere[13]. Thus, we only provide here a brief summary of the spectrometer. Since UA8 was installed in the same interaction region as the UA2 experiment[14] and a common data acquisition system was used[13], the data from the UA2 calorimeter system could be used offline to study the X system in React. 1.

2.1 Roman-pot spectrometers

The Roman-pot spectrometers, which used the low-β machine quadrupole magnets, consisted of four pot installations positioned in each arm of intersection LSS4 at the CERN S$p\bar{p}$S-Collider. The positions of the pots in one spectrometer are shown in Fig. 4. The four spectrometers are labled according to which arm they are in (P for outgoing proton and M for outgoing antiproton), and whether they are above or below the beam pipe ("U" for "Up" and "D" for "Down"). Thus, the "Up" spectrometer in the proton arm is called PU. If a track is in a "Down" spectrometer, we define the "adjacent" spectrometer to mean the "Up" spectrometer of the same arm. Similarly, we define "opposite" spectrometer to be the one diagonally opposite the one containing a trigger particle (i.e., in the other arm).

Figure 4 shows inelastic ($x_p \sim 0.95$) particle trajectories through one of the spectrometers. The shaded region shows the allowed trajectories for elastic scattering. The final state proton or antiproton momentum is calculated using the reconstructed vertex position (if it exists), given by the UA2 central chamber system and points reconstructed from hits in chambers 1, 2 and 3. Chamber 4 was also used in the fit, if a track traversed it.

The UA4 experiment[16], in their measurements of elastic and diffractive scattering[17, 18], used similar pot installations in LSS4, but without a pot upstream of the first quadrupole magnets. With this first measuring station, our installation yielded acceptance for leading protons and antiprotons with x_p as small as 0.70.

A system of wire chambers was equipped with high bandwidth readout electronics which interfaced to a 240 MIPS (Million Instructions per Second) data-driven trigger

processor[13, 19] for calculating the proton or antiproton momentum online. High speed, efficient triggering was necessary because we were interfaced to the UA2 data acquisition system and were required to present only minimum perturbation to that experiment.

As discussed in Ref. [13], each chamber contains 6 planes with 2 mm wire spacing in a conventional MWPC configuration. There are 2 planes with horizontal wires, y and y' (shifted half a cell), and two sets of $\pm 7°$ stereo views (with respect to the horizontal), u, u' and v, v'. With a 4-bit time-to-digital converter (5 ns least count) on each wire, a chamber provides $\sim 65\,\mu$m position resolution in the vertical (bending) plane.

Figure 5 shows a "beams-eye" view of the UA8 chamber aperture which is closest to the center of the interaction region. The four-lobed curve in the figure illustrates the contour of the beam pipe which follows that of the quadrupole-magnet pole pieces. The overlap between the beam pipe and rectangular chambers above and below the beam illustrates the limited azimuthal range through which a particle may pass. A discussion of the acceptance corrections for the resulting losses is given below in Sect. 3.4. Data were recorded with the bottom edge of each pot set, in different runs, at either 12 or 14 beam widths from the beam axis. The combined data sample is referred to below as the "12σ and 14σ" data.

The Roman-pot spectrometers in the $\bar{p}$-arm were also used in a stand-alone mode for inclusive measurements[20, 13] of $\bar{\Lambda}$ production for $x_\Lambda > 0.7$.

2.2 Spectrometer resolutions

Figure 6 shows the momentum distribution of tracks in elastic scattering events (events with two collinear tracks, no evidence of other tracks in the event, and no energy in the UA2 calorimeter system) with a Gaussian curve fitted to the data. The fitted σ = 1.95 GeV, or $\sigma(x_p) = 0.0061$, implies a resolution in diffractive mass, of $\sigma(\sqrt{s'}) = 1230/\sqrt{s'}$ GeV. This resolution improves with increasing scattering angle, approximately as $0.0077/|t|$, due to the characteristic field shape of the quadrupole magnets.

The resolution in momentum transfer, t, is dominated by the dispersion of the incident beams resulting from the low-β injection. The beam dispersions have been calculated to be 180 μrad and 150 μrad in the vertical planes of the p and $\bar{p}$ beams, respectively. Since the scattering angle in the vertical plane, 3–5 mrad, is much greater (for accepted particles) than the average scattering angle in the horizontal plane, 0.2 mrad, the vertical component dominates the uncertainty. This leads to a p_t uncertainty of about 0.052 GeV, and t uncertainties from 0.10 to 0.15 GeV^2 in the range, $1.0 < -t < 2.2$ GeV^2.

An additional t-scale uncertainty exists due to the uncertainty in the absolute vertical position of the Roman-pots relative to the beam line. This position uncertainty is estimated to be less than 300 μm, which corresponds to a 23 μrad shift in the average measured angle or to t-scale shifts of 0.014 to 0.021 GeV^2 in the range, $1.0 < -t < 2.2$ GeV^2. From all t uncertainies, there is a combined systematic cross section uncertainty of about 6%.

2.3 UA2 calorimeter and time-of-flight counters

Figure 7 shows the UA2 calorimeter system after the upgrade[14], in which end-cap calorimeters were added to increase the acceptance in laboratory polar angle to $6° < \theta < 174°$. The central calorimeter covers the full azimuthal range, with twenty-four $15°$ cells in ϕ, and $140° > \theta > 40°$ with ten $10°$ cells in θ. The end-cap calorimeters each adds 8 cells in θ and also covers the full range of azimuthal angle. A tower structure is used which points to the center of the interaction region.

Figure 7 also shows the UA2 time-of-flight (TOF) counters, which cover the ranges $2°$–$12°$ and $168°$–$178°$ (with pseudorapidity, $2.3 < |\eta| < 4.1$). As discussed below in Sect. 3.2, when used offline together with the UA2 calorimeter information, these counters offered us a means to define various classes of event topologies. For example, these counters were found to be very useful as offline vetoes, for defining pseudorapidity gaps in both arms as a signature of double-$\mathcal{P}$omeron-exchange[21].

The use of the updated version of the UA2 detector simulation software[22], with which we could simulate observed data for any assumed physics model, was very important in all analyses involving data from the UA2 detectors.

2.4 Data acquisition trigger

The trigger logic used to record examples of React. 1 contained the following components:

- The wire chamber data were used in the data-driven trigger processor, as described in the following paragraphs, to determine that a valid track existed in at least one spectrometer.

- The scintillation counters were used to veto events that had: (a) beam halo tracks, or (b) hits in a spectrometer adjacent (i.e. in the same arm) to one with a valid track.

The data-driven trigger processor[13, 19] required that there be either one hit or two contiguous hits in the y and y' planes in each of the first three chambers of a spectrometer. Moreover, the y and y' hits in each plane were required to have sufficient proximity to be consistent with the passage of a single track through the chamber. If these conditions were satisfied, the processor calculated the momentum from the tracks passage through the quadrupole magnet(s).

The online momentum resolution of the trigger processor is illustrated in Fig. 8 which shows the difference between the offline and online momentum calculations for a sample of proton trigger events. The Gaussian fit with $\sigma = 4.4$ GeV corresponds to a processor momentum resolution of 1.4%. The fact that this resolution is worse than the offline resolution of 0.6% stems from the facts that the processor momentum estimate is based on second-order transport equations through the magnets and that the primary vertex point was not used in the online algorithm. Furthermore, the offline estimate benefits from improved chamber alignment and drift time corrections. However, there is no reason

why an improved online algorithm could not be used in any future experiment of this type. The distribution in Fig. 8 does not peak at zero because of small errors in the chamber positions which were used to compute the tables used online in the processor.

The trigger was set to select tracks with x_p in the range 0.70 to 1.05. The trigger processor decreased the trigger rate by a factor of ≈ 150 from the raw scintillator coincidence rate, with no significant loss of good proton events.

For each spectrometer, scintillation counter signals were used to veto events with beam halo tracks by demanding that there be no counter hit in planes 1 or 2 of the diagonally opposite spectrometer, which had the timing of an incoming beam bunch.

The data recorded for React. 1 relied entirely on the Roman-pot spectrometers and made no requirements on any of the UA2 detectors. However, the UA8 trigger was OR'ed with the normal UA2 triggers and all UA8 and UA2 detector data were written out to UA2 data tapes for each UA8 trigger. Thus, in the offline analysis, the UA2 detector information was available for each example of React. 1.

3   Event selection and corrections

3.1   Event selection and background sources

Table 1 shows how the event data sample[23] is reduced with each of the offline selection cuts. Of the initial event sample of 150,000 triggered events (combined 12σ and 14σ), 59% of all triggers are found with one reconstructed track which has $x_p > 0.9$ (this fraction would have been much larger, had we increased the lower limit of $x_p > 0.7$ imposed in the trigger processor). A small number of these events (1.7%) had hits in the adjacent spectrometer and were rejected. Since this cut was in the hardware trigger, the offline cut serves to remove veto inefficiencies.

10.5% of these events contain evidence that two or more interactions occurred in the same bunch crossing ("pileup") and are removed from the event sample[4]. In the accepted events, the UA2 and UA8 time-of-flight information is required to be consistent with the single event hypothesis, at most one vertex is found using the UA2 silicon detectors, and the total visible longitudinal momentum (calorimeter + spectrometer) in the trigger hemisphere is less than the maximum possible beam momentum (taking resolution into account).

A further cut removed 14.0% of the remaining events because of contamination from beam halo tracks. This cut, which is described in more detail in Ref. [13], is based on the timing information of hits in the chambers of the diagonally opposite spectrometer, which is characteristic of a halo track passing through the entire spectrometer system. Other evidence for halo contamination can be obtained from observation of the transverse position of an event vertex (or from the transverse positions of the tracks at z = 0, if no

---

[4]In the rejected events, a measured p or $\bar{p}$ from a bona fide example of React. 1 has associated calorimeter information which is augmented by particles from a different event.

vertex is found). The final cut, called "Energy Topology" in Table 1, is described in the next section.

Figure 9 displays the uncorrected distribution in momentum transfer, t, for the final sample of 63K events with $x_p > 0.9$. The distribution reflects the smooth acceptance function defined below. Figure 10 shows the corresponding uncorrected x_p distributions for several ranges of t. There is seen to be a small improvement in the resolution in the high $|t|$ region due to the quadrupole field shape.

Figure 11 shows the invariant mass of the portion of the X system in React. 1 which was contained in the UA2 calorimeter[5]. Due to incomplete polar angle coverage of the calorimeter system, particles can completely miss the calorimeter at small angles, resulting in a calculated invariant mass which is less than $\sqrt{s'}$. In particular, the peak at zero mass in Fig. 11 is due to low-mass diffractive events whose particles in the diffractive system are all sharply collimated forward, opposite the observed proton.

3.2   Use of energy-flow topology in event selection

The availability of the data from the UA2 calorimeter and time-of-flight (TOF) counters (pseudorapidity range $2.3 < \eta < 4.1$) in the offline analysis allows us to study the energy-flow topology of the diffractive system. Such information permits the removal of certain types of background, such as when the measured diffractive mass, $\sqrt{s'}$, is inconsistent with the observed energy-flow topology. This can occur, for example, if the observed p or $\bar{p}$ is not alone at the lower vertex in Fig. 3.

Figure 12 shows the fractions of all events which have hits in the four combinations of trigger-side and opposite-side TOF counters, plotted vs. diffractive mass, $\sqrt{s'}$. These four possible combinations of struck TOF counters are as follows:

- NY: ("No-Yes") Trigger-side counters not hit; opposite-side counters hit.

- YN: Trigger-side counters hit; opposite-side counters not hit.

- YY: Both trigger-side and opposite-side counters hit.

- NN: No TOF counters hit.

The dominant patterns in Fig. 12 are seen to be NY and YY. As expected, NY dominates for low mass diffraction; NN is a smaller subset of the physics of NY, when a low-mass diffractive system is forward at such a small angle that its tracks miss the TOF counters. YY dominates at high mass, corresponding to a forward cone of particles which increasingly spreads out into the trigger hemisphere at larger mass. In addition, however, there is the smaller component, YN, in which only counters on the trigger side are hit.

In order to further understand the topologies of these events, we use the calorimeter information and define the variable, θ_{cal}, which for each event is the polar angle in the

---

[5]The calorimeter invariant mass is estimated for each event by assuming that non-zero energy in each "struck" cell of the calorimeter is caused by a massless particle and then calculating, $M_X^2 = (\Sigma E_i)^2 - |\Sigma \vec{P}_i|^2$, summing over all cells.

laboratory of the vector sum of its calorimeter energy vectors (the energy in each cell is treated as a vector).

Figures 13 and 14 show histograms of θ_{cal} for each of the TOF patterns, for two event samples, the first (low-mass) selected from the center of the diffractive peak at $x_p \sim 1$ and the second with $\sqrt{s'} = 130$ GeV ($x_p = 0.043$). At low mass, the NY event sample is dominant with a clear forward peak in θ_{cal} (hits opposite the trigger proton). A forward peak also exists at low mass in the NN sample, corresponding to events in which high momentum tracks in the diffractive system have $\eta > 4.1$, some low momentum tracks hit the calorimeter cells at small angles ($\eta < 2.3$), but the opposite-side TOF counters are not hit. A very small and inconsequential signal exists in the YY class, where the trigger proton is accompanied by one or more low energy tracks which hit the same-side TOF counters.

In the higher mass sample with $\sqrt{s'} = 130$ GeV in Fig. 14, the YY and NY topologies dominate with clear peaks in the θ_{cal} distributions opposite the trigger particle. As expected, this is due to a spreading of lower momentum particles from the diffractive system into the trigger-side hemisphere at higher mass. However, a new class of events occurs in Fig. 14. In the YN and NN samples, where the TOF counters in the opposite arm have no hits, θ_{cal} is peaked on the trigger side. We identify this effect with diffractive excitation on the trigger side. As such, these events constitute a class of background events and are removed from our data sample in Table 1 if $\theta_{\mathrm{cal}} < 90°$.

We can compare the dominant NY and YY events with a Monte Carlo model[24] of longitudinal (or p_t-limited) diffractive excitation (see Section 6). Figure 15 shows θ_{cal} for NY and YY events at $\sqrt{s'} = 130$ GeV, which have total transverse calorimeter energy in the range, $5 < \Sigma \mathrm{E_t} < 10$ GeV. Good agreement is seen between data and Monte Carlo, except at small θ_{cal}, where there appears to be a small excess of events over the Monte Carlo calculation. This could be due to a residual background from double-diffractive events, where the opposite side diffractive system strikes the TOF counters.

3.3   Efficiencies for trigger and selection cuts

Table 2 lists the individual efficiencies for the trigger components discussed in Sect. 2.4, as well as for the pileup and halo offline cuts listed in Table 1.

The two trigger processor corrections were determined by the combined use of processor emulation in the UA8 detector simulation Monte Carlo program and by offline analysis of data recorded without using the processor in the trigger. The two small corrections for accidental vetoes were estimated from the measured halo and noise rates, respectively.

Events with a good spectrometer track (i.e., not beam halo), which are removed from the sample by the offline pileup selection described in Sect. 3, are corrected for in the cross section evaluation. This is accomplished by determining how many events in the pileup-rejected event sample have good spectrometer tracks. Figure 16 shows the fraction of events in the total sample which survive the pileup cut as a function of track x_p. Although the average loss due to pileup is 9.2%, we use the distribution shown in Fig. 16 to obtain the final cross section numbers given below.

9

The fraction of good events that are accidentally rejected by the offline halo veto is given by the number of halo-rejected events with a single vertex (as determined using the UA2 silicon detectors), which pass the pileup cut, divided by the total number of single-vertex events. This fraction is 8.4%.

3.4 Geometric acceptance corrections

Monte Carlo detector simulation software was written to correct for all geometric acceptance and detector inefficiencies. It was also used to estimate resolution effects whose origins are related to effects such as: t_o-jitter in the chamber TDC system, time slewing, digitization bins and trigger requirements. The simulated data were passed through the normal pattern-recognition software for decoding and analysis, with the identical procedures used in the processing of real data. The resulting resolutions in chamber spatial measurements, elastic momentum and other variables are in good agreement with those observed in the real data.

Figure 17 shows the geometric acceptance at several t-values plotted vs. x_p for the MU spectrometer. In this figure, the geometric acceptance is defined as the fraction of all antiprotons produced in the antiproton arm with a specific x_p and t which is detected and reconstructed by the MU spectrometer. These acceptances are found to vary smoothly over the x_p and t ranges covered in this paper.

4 Absolute cross sections

4.1 Differential cross section vs. x_p and t

The inclusive single diffractive differential cross section, $\frac{d^2\sigma}{d\xi dt}$, has been evaluated in the x_p range, 0.91–0.97, where the upper limit is chosen to avoid resolution "smearing" from the peak at $x_p \approx 1$. This point is demonstrated by the dashed curve in Fig. 1 which is approximately a mirror image of the event distribution with $x_p > 1.0$, the existence of which is a pure resolution effect.

$\frac{d^2\sigma}{d\xi dt}$ was evaluated at points in $\xi = 1 - x_p$ and t space, independently for each of the three spectrometers, PU, PD and MU (the fourth spectrometer was not used for the analysis reported here). The resulting weighted averages at each point are given in Table 3.

The average-t values calculated for the events in each t-bin show no systematic shifts as a function of x_p and the average values are close enough to the bin center values that the bin centers are used in the analyses described below.

Figure 18 compares our $\frac{d^2\sigma}{d\xi dt}$ values in the t-bin, 1.1–1.2 GeV^2 with measurements in the same range at the S$p\bar{p}$S-Collider[17] (UA4 experiment) and at the CERN Intersecting Storage Rings[15]. The UA4 points are in reasonable agreement with our UA8 points, while the ISR cross sections are somewhat larger, on the average. As will be shown in Sect. 5.3, the s-dependence of $\frac{d^2\sigma}{d\xi dt}$ at fixed $\xi = s'/s$ and t directly exhibits the s'-

dependence of the $\mathcal{P}$omeron-proton total cross section, wherever non-$\mathcal{P}$omeron-exchange background can be ignored. It is seen that the $\mathcal{P}$omeron-proton total cross sections at $\sqrt{s'} = \sim 6$ Gev and ~ 100 GeV are the same within about $\sim 20\%$.

In our analyses, we make use of published $\frac{d^2\sigma}{d\xi dt}$ data from the following experiments:

- FNAL fixed target: Schamberger et al.[25], $s = 262, 309, 366, 565, 741$ GeV^2.

- FNAL fixed target: Cool et al.[26], $s = 189, 377$ GeV^2.

- FNAL fixed target: Akimov et al.[27], $s = 294, 700$ GeV^2.

- CERN ISR: Albrow et al. (CHLM Collaboration)[15], $s = 551, 930$ GeV^2.

- CERN S$p\bar{p}$S-Collider: Bozzo et al.(UA4 Collaboration)[17], $s = (546)^2$ GeV^2.

- FNAL Tevatron: Abe et al.(CDF Collaboration)[28], $s = (546)^2, (1800)^2$ GeV^2 (*Fitted function only*).

The main triple-Regge analysis reported below is done by simultaneously fitting our UA8 data and the ISR data of Albrow et al.[15]. This procedure is dictated by the large amount of tabulated data available in Refs. [15] over a wide range of momentum transfer and our wish to avoid using the lower energy data where resonance effects distort the cross section (see Sect. 5.6).

4.2   Total single diffractive cross section, σ_{sd}^{total}

Due to resolution smearing in x_p, it is not possible for us to quote differential cross sections for $x_p > 0.97$. However, the cross section integrated over x_p, $d\sigma/dt$, can be evaluated because the acceptance depends weakly on x_p in this region. It is conventional to quote $d\sigma/dt$ for $x_p > 0.95$, because the integral background from non-$\mathcal{P}$omeron exchange throughout this region can be ignored.

The resulting (single arm) values of $d\sigma/dt$ are given in Table 4. They are plotted in Fig. 19, together with the corresponding measurements from the UA4 experiment[17, 18] at the nearby energy of $\sqrt{s} = 546$ GeV at the S$p\bar{p}$S-Collider. The UA4 points come from two independent runs, one at high-β and one at low-β which allowed them to span most of the available t-range. The UA8 and UA4 points are seen to be in good agreement in the region where they overlap. The solid curve superimposed on the points is to "guide-the-eye". UA4 obtains[18] a total single diffractive cross section (both arms) of (9.4 ± 0.7) mb, or 4.7 ± 0.35 mb for a single arm.

Figure 20, taken from Ref. [29], shows a survey of existing measurements of σ_{sd}^{total} (for both arms) with $x_p > 0.95$, as a function of $\sqrt{s}$. The points at $\sqrt{s} = 13.8$ and 19.4 GeV are the Fermilab fixed-target measurements of Cool et al.[26] at proton beam momenta of 100 and 200 GeV, respectively. A third Cool et al. point, marked $p\bar{p}$, is from data taken with a $\bar{p}$ beam. At higher energy, there are the measurements at the CERN Intersecting Storage Rings[30, 31] and, at the still higher energies of $\sqrt{s} = 546$ and 1800 GeV, there are the measurements from the UA4, CDF[28] and E710[32] experiments.

Goulianos[29] has drawn attention to the remarkable behavior of the total single diffractive cross section, σ_{sd}^{total}, as a function of energy. The observed total single diffractive cross section does not continue to increase following the expected triple-Regge behavior (see Sect. 5.1), which is well known to violate unitarity. The observed flattening of σ_{sd}^{total} for c.m. energies above about 20 GeV is associated[29] with a saturation of the flux factor, $F_{\mathcal{P}/p}(t, \xi)$.

The solid line in Fig. 20 represents an attempt[29] to describe the observed s-dependence of σ_{sd}^{total}. $\sigma_{\mathcal{P}p}^{total}$ is assumed throughout to follow the high-energy triple-$\mathcal{P}$omeron form: $\sigma_{\mathcal{P}p}^{total} = \sigma_0 (s')^\epsilon$. Below $\sqrt{s} = 22$ GeV, the normalization constant, K, in $F_{\mathcal{P}/p}(t, \xi)$ is assumed to be constant, following conventional wisdom. However, when s exceeds $\sqrt{s} = 22$ GeV, K is forced to decrease with increasing s, in order to account for the flattening of σ_{sd}^{total}. This is accomplished by dividing K by the integral over ξ and t of the Flux Factor. In the following section, one of our principal concerns is to determine whether the consequences of this prescription are in agreement with the measured differential cross section, $\frac{d^2\sigma}{d\xi dt}$ in React. 1.

5 Analysis

In this section, we present a triple-Regge analysis of the UA8 data together with the extensive measurements by the CHLM collaboration[15] at the CERN Intersecting-Storage-Rings. We explore the significance of the the fact that the differential cross sections for React. 1 at the ISR and at the S$p\bar{p}$S-Collider have similar magnitudes. We present a parametrization that describes all the data.

In the following sections, after summarizing the triple-Regge phenomenology which describes diffraction, we obtain values of the effective $\mathcal{P}$omeron Regge trajectory in the $|t|$–range, 1.0–1.6 GeV^2, which shows a strong departure from linearity, with a flattening as $|t|$ increases.

We then examine the s-dependence of $\frac{d^2\sigma}{d\xi dt}$ at fixed ξ and t, which is seen to directly reflect the s'-dependence of $\sigma_{\mathcal{P}p}^{total}$ multiplied by the normalization of $F_{\mathcal{P}/p}(t, \xi)$, K. The data are seen to have a behavior that is inconsistent with the s-dependent normalization constant, $K(s)$, proposed by Goulianos[29]. We also show that two components are required in $\sigma_{\mathcal{P}p}^{total}$, corresponding to the triple–$\mathcal{P}$omeron ($\mathcal{PPP}$) and $\mathcal{P}$omeron–$\mathcal{P}$omeron–Reggeon ($\mathcal{PPR}$) terms in the triple-Regge expansion.

Next, we present the results of successful fits to the combined data over the ξ range, 0.03–0.09. These fits are first done in the range, $\xi = 0.03$–0.04, where the non-$\mathcal{P}$omeron-exchange background is small and therefore neglected, and then over the extended range, where the non-$\mathcal{P}$omeron-exchange background is taken into account. The two types of fits are found to agree. The requirement of a second term in $\sigma_{\mathcal{P}p}^{total}$ is reinforced by the fits. This is similar to what is needed to describe real-particle total cross section data. Independent confirmation of the nonlinear $\mathcal{P}$omeron trajectory is also obtained from the fits. We show that the non-$\mathcal{P}$omeron-exchange background in the differential cross sections cannot be accounted for by one-pion-exchange. Finally, we show that the triple-Regge formula is

deficient in describing data at low diffractive mass and energy (resonance region).

5.1 Triple-Regge phenomenology of diffraction

Mueller's[33] generalized optical theorem allows Regge analyses to be performed on inclusive processes such as React. 1. At small ξ and $s' >> 1$, the Mueller approach yields a differential cross section of the form (see, for example, Ref. [34]):

$$\frac{d^2\sigma}{d\xi dt} = \sum_{ijk} G_{ijk}(t) \cdot \xi^{1-\alpha_i(t)-\alpha_j(t)} \cdot (s')^{\alpha_k(0)-1} \qquad (3)$$

s' is in units of GeV^2. $\alpha_i(t)$ is the Regge trajectory for Reggeon i. The sum is taken over all possible exchanged Reggeons in the diagram shown in Fig. 21. The $G_{ijk}(t)$ are products of the various Reggeon-proton and triple-Reggeon couplings in Fig. 21 (and the signature factors).

Because the $\mathcal{P}$omeron is the highest-lying trajectory (has intercept slightly larger than unity at $t = 0$), when $i = j = \mathcal{P}$omeron, $1 - 2\alpha < 0$ and the differential cross section increases rapidly as $\xi \to 0$. This corresponds to the empirical observation that the most likely momentum fraction of the $\mathcal{P}$omeron in the proton, ξ, is near zero.

There are two dominant terms at small ξ, namely $ijk = \mathcal{PPP}$ and $\mathcal{PPR}$. As discussed in Sect. 1, it has become customary to rewrite Eq. 3 as a product of a $\mathcal{P}$omeron flux factor, $F_{\mathcal{P}/p}(t, \xi)$, in the proton (a measure of the probability to find a $\mathcal{P}$omeron in a proton with momentum transfer, t, and momentum fraction ξ) and a $\mathcal{P}$omeron-proton total cross section, $\sigma_{\mathcal{P}p}^{total}$. The forms of $F_{\mathcal{P}/p}(t, \xi)$ and $\sigma_{\mathcal{P}p}^{total}$ are as follows:

$$\frac{d^2\sigma_{sd}^{total}}{d\xi dt} = F_{\mathcal{P}/p}(t, \xi) \cdot \sigma_{\mathcal{P}p}^{total}(s') = [K|F_1(t)|^2 e^{bt} \xi^{1-2\alpha_{\mathcal{P}}(t)}] \cdot \sigma_0[(s')^{\epsilon_1} + R(s')^{\epsilon_2}] \qquad (4)$$

where $|F_1(t)|^2$ is the standard Donnachie-Landshoff[35] form-factor[6] (see comment at the end of this section on the reason for the e^{bt} term). The squared diffractive mass, $s' = \xi s$. The quantity, ϵ, is defined as, $\alpha(0) = 1 + \epsilon$.

We note the following:

- In Eq. 4, $|F_1(t)|^2 \cdot e^{bt}$ carries the t-dependence of the G_{ijk} in Eq. 3. The same t-dependence is assumed for both $G_{\mathcal{PPP}}$ and $G_{\mathcal{PPR}}$. Physically, this is saying that the $\mathcal{P}$omeron has the same flux factor in the proton, independent of whether there is $\mathcal{P}$omeron-exchange or Reggeon-exchange in the $\mathcal{P}$omeron-proton interaction.

- Expressing $\sigma_{\mathcal{P}p}^{total}$ as the sum of two components is in direct analogy to all total cross sections, which are fit[36, 37, 38] by the same 2-component Regge function:

$$\sigma_{\mathcal{P}p}^{total}(s') = \sigma_0[(s')^{\epsilon_1} + R(s')^{\epsilon_2}] \qquad (5)$$

---

[6] $F_1(t) = \frac{4m_p^2 - 2.8t}{4m_p^2 - t} \cdot \frac{1}{(1-t/0.71)^2}$

The first term corresponds to the triple-$\mathcal{P}$omeron process, ($\mathcal{PPP}$), while the second corresponds to other non-leading, C=+ (a/f_2), trajectories in the $\mathcal{P}$omeron-proton interaction, the $\mathcal{P}$omeron-$\mathcal{P}$omeron-Reggeon process ($\mathcal{PPR}$). The latter term is largest at low energies and decreases with increasing s. We shall see below that there is good evidence that the $\mathcal{PPR}$ term is required by the data. Donnachie and Landshoff[36] determined the "effective" ϵ values to be 0.08 and -0.45, respectively, from fits to the s-dependence of available total cross section data. However, recent analyses[37, 38] and new data yield somewhat different values and, in the fits reported here, we use[7] $\epsilon_1 = 0.10$ and $\epsilon_2 = -0.32$. R is a free parameter.

- The product, $K \cdot \sigma_0$, is the magnitude of $G_{\mathcal{PPP}}$, and the product, $K\sigma_0 R$, is the magnitude of $G_{\mathcal{PPR}}$. Since the overall normalization constant, K, of $F_{\mathcal{P}/p}(t,\xi)$ is not uniquely defined theoretically, and since it multiplies $\sigma_{\mathcal{P}p}^{total}$ in Eq. 4, only the product, $K \cdot \sigma_0$ is measurable. This is one of the free parameters in our fits.

- The "standard" $\mathcal{P}$omeron Regge trajectory, determined from low momentum transfer data, is linear: $\alpha(t) = 1 + \epsilon + \alpha' t$, with the slope[35]: $\alpha' = 0.25$ GeV^{-2}. However, we show in the next section that this linear trajectory is too small in the 1–2 GeV^2 $|t|$ -region of this experiment to adequately describe the data, and we allow for a quadratic term in the trajectory:

$$\alpha(t) = 1.10 + 0.25t + \alpha'' t^2 \qquad (6)$$

- The multiplicative factor , e^{bt}, is found to be required by the data to compensate for the presence of the quadratic component in the $\mathcal{P}$omeron trajectory. The introduction of this factor is not sacrilegious, because $|F_1(t)|^2$ has never been shown to describe React. 1 at large $|t|$. Although Donnachie and Landshoff have suggested[12] that $\sigma_{\mathcal{P}p}^{total}$ may also depend on momentum transfer, t, we ignore that possibility in this paper but note that any such dependence would be absorbed in the e^{bt} factor.

5.2 Measurement of the effective $\mathcal{P}$omeron trajectory

In order to determine the effective $\mathcal{P}$omeron trajectory at given values of t, we fit to the uncorrected data points with $x_p > 0.97$ in Figs. 10. The appropriate function is found by noting that, at a fixed momentum transfer t, Eq. 4 can be written as:

$$\frac{d^2\sigma}{d\xi dt} \propto \xi^{1-2\alpha(t)} \cdot \sigma_{\mathcal{P}p}^{total}(\xi s) \qquad (7)$$

where we recall that $s' = \xi s$. It is evident that the explicit functional dependence of $\sigma_{\mathcal{P}p}^{total}$ on ξ plays a significant role in the fits. With the use of Eq. 5, we rewrite Eq. 7 as:

$$\frac{d^2\sigma}{d\xi dt} \propto \xi^{1-2\alpha(t)+\epsilon_1} + R \cdot s^{\epsilon_2-\epsilon_1} \cdot \xi^{1-2\alpha(t)+\epsilon_2} \qquad (8)$$

---

[7]We do not have sufficient constraints with our data to allow ϵ_1 and ϵ_2 to be free parameters.

$$\frac{d^2\sigma}{d\xi dt} \ \propto \ \xi^{1.10-2\alpha(t)} \ + \ 0.0178 \cdot \xi^{0.68-2\alpha(t)} \tag{9}$$

In evaluating the constants in Eq. 8, we assume $R = 4.0$ (see Sect. 5.4), $\epsilon_1 = 0.10$ and $\epsilon_2 = -0.32$, leading to Eq. 9. Fitting this function to data in the $x_p \sim 1$ peak region in a given t-bin yields the value of α at that t-value. To perform the fits, Monte-Carlo events were generated according to the function, then multiplied by the acceptance function and offline selection efficiencies and smeared according to the experimental resolution.

The traditional fit to the differential cross section in the peak region, using the function ξ^m, ignores the $\mathcal{PPR}$ term in Eq. 8, which is negligible at large ξ and s. However, in fits at small ξ, where the second term is significant, we have performed our fits both with and without it. We note that the fits themselves do not distinguish between the two cases. The evidence that the data require both terms is given in Sect. 5.4.

Table 5 contains values of $\alpha(t)$ obtained with and without the $\mathcal{PPR}$ term. The resulting $\alpha(t)$ values for both types of fits are plotted vs. t in Fig. 22. The fits using the 2-component $\sigma_{\mathcal{P}p}^{total}$ are shown in Fig. 23. We have fit only in the range, $1.0 < -t < 1.6$ GeV^2, where our experimental resolution is best understood.

The α values obtained with the 2-component cross section are seen to be systematically lower by about 0.05 than those obtained with the 1-component cross section. This can be understood with reference to Fig. 24, which shows the two components in one of the fits plotted separately. Since the second component is largest at small ξ, its x_p distribution drops off much more rapidly on the low side of the peak. Thus, a fit without the second component included requires a larger value of α to fit to the same shape data distribution.

The shaded region in Fig. 22 results from the global fits to all UA8 and ISR data in the ξ-range, 0.03–0.09, as described in Sec. 5.4. We note that the (2-component) points and the shaded band are in essential agreement, even though they are obtained by analyzing different data with different methods. They demonstrate that the $\mathcal{P}$omeron trajectory departs from linearity in our t-region and is substantially larger than the linear function. Frankfurt and Strikman[39] and Collins et al.[40] have pointed out that such an increasing effective trajectory may arise from the onset of the perturbative two-gluon $\mathcal{P}$omeron. Another possibility[41, 42] is that the exchange of two $\mathcal{P}$omerons (or more) might be responsible for such an effect. It is well known that two-$\mathcal{P}$omeron-exchange plays an important role in understanding elastic scattering[35].

5.3 s-Dependence of $\frac{d^2\sigma}{d\xi dt}$ at fixed ξ and t

From the differential cross section, Eq. 4, we see that, at fixed ξ and t, and because $s' = \xi s$, the differential cross section directly displays the s-dependence of $\sigma_{\mathcal{P}p}^{total}(s')$ multiplied by any possible s-dependence of K[29].

$$\frac{d^2\sigma}{d\xi dt} \ \propto \ K \ \cdot \ \sigma_{\mathcal{P}p}^{total}(\xi s) \tag{10}$$

We first consider the ξ-range, 0.03–0.04:

- $\xi > 0.03$ is suffcently far from the large peak near $\xi \sim 0$, that resolution smearing does not distort the observed distribution.

- Background from non-$\mathcal{P}$omeron-exchange is small, 15% or less in this region[43] and is the size of the data points on the plots. Thus, for our initial fits, we can ignore it. The analysis of the full data set, as described in Sect. 5.4 is consistent with a background of this magnitude.

Figure 25 shows what is expected for the s-dependence of $\frac{d^2\sigma}{d\xi dt}$ for the four combinations of possibilities, with and without an s-dependence of K, and with and without the $\mathcal{PPR}$ term in $\sigma_{\mathcal{P}p}^{total}$. The behaviors seen in Fig. 25 are easily understood:

- 1-component $\sigma_{\mathcal{P}p}^{total}$ and constant K: $\quad \frac{d^2\sigma}{d\xi dt}$ increases uniformly according to $s^{0.10}$

- 2-component $\sigma_{\mathcal{P}p}^{total}$ and constant K: $\quad \frac{d^2\sigma}{d\xi dt}$ initially decreases because of the $s^{-0.32}$ term, and then increases because of the $s^{0.10}$ term.

- 1-component $\sigma_{\mathcal{P}p}^{total}$ and $K(s)$: $\quad \frac{d^2\sigma}{d\xi dt}$ initially increases according to $s^{0.10}$, and then decreases above $\sqrt{s} = 22$ GeV because of the "renormalization" of K[29].

- 2-component $\sigma_{\mathcal{P}p}^{total}$ and $K(s)$: $\quad \frac{d^2\sigma}{d\xi dt}$ initially decreases because of the $s^{-0.32}$ term. Above $\sqrt{s} = 22$ GeV, the presence of the decreasing term coupled with the "renormalization" of K leads to a rapidly decreasing behavior.

It is evident that data should easily distinguish between the four cases.

Figures 26(a-c) show the available experimental values of $\frac{d^2\sigma}{d\xi dt}$ vs. s at $\xi = 0.035$ and at three fixed values of t. The weak dependence on s of the $-t = 1$ GeV^2 ISR and UA8 data points in Fig. 26(a) reflects what we have already seen in Fig. 18. The solid curves are triple–Regge predictions for case (ii) and are discussed in the following section.

At the two lower $|t|$ values, which approximately span the region where CDF has their data, points from the CDF collaboration[28] are calculated from their fitted function[8]. See also Fig. 27. We note that the two CDF points are not self-consistent (their fitted t-slopes are (7.7 ± 0.6) GeV^{-2} and (4.2 ± 0.5) GeV^{-2}, at $\sqrt{s} = 546$ GeV and 1800 GeV, respectively; the latter is in excellent agreement with $|F_1(t)|^2$ in Eq. 4. However, we note that, at $|t| = 0.05$ GeV^2, where the different $|t|$-slopes have much less effect, the 546 and 1800 GeV data display the increase with energy predicted by the solid curve.

We also note that, at low $|t|$ in Figs. 26(b,c), the Schamberger et al. points[25] are systematically larger by 10–15% than *both* the Cool et al.[26] and Albrow et al.[15] points. Nonetheless, it is evident from a comparison of Fig. 25 with Fig. 26 and 27, that the data are inconsistent with all cases where $\sigma_{\mathcal{P}p}^{total}$ has a single component, and/or where $K(s)$ follows the "renormalization" procedure of Goulianos[29].

---

[8]However, since their quoted background levels are larger than in other experiments, where the background in the ξ-region shown is small enough to be ignored, we show the sum of their fitted "signal" and "background".

5.4 Combined fits to UA8 and ISR data

To test the validity of Eqs. 4 and 5 we fit our UA8 data simultaneously with the ISR data[15]. In our first fit, we continue to focus on the narrow ξ-range, 0.03–0.04, where experimental resolution and non-$\mathcal{P}$omeron-exchange background issues do not play a significant role and are ignored in our analysis. Figure 28 shows the mean $\frac{d^2\sigma}{d\xi dt}$ in the range $\xi = 0.03$–0.04 plotted vs. $|t|$, for each of four data sets (there are two sets of ISR measurements at $s = 930$ GeV^2).

Table 6 shows the results of fitting Eqs. 4 and 5 to all available data points in the $\xi = 0.03$–0.4 range, with various combinations of free parameters in the fits. It is clear that, in order to have an acceptable χ^2/Degree of Freedom, α'', b and R are all required. The last fit in the table, in which all three parameters are included, is shown superimposed on the data in Figs. 28 and is seen to be quite good.

One of the remarkable results of the fit is that $R \neq 0$. This shows that the $\mathcal{PPR}$ term is required by the data, as discussed in the previous section.

A second remarkable result of the fit is that the value of $\alpha'' = (0.078 \pm 0.013)$ GeV^{-4} leads to a $\mathcal{P}$omeron trajectory, plotted as the shaded band in Fig. 22, which is in good agreement with the values obtained from the 2-component fits to the small-ξ peaks in Figs. 23. This result reinforces our conclusion that the $\mathcal{P}$omeron trajectory flattens in our t-range and also lends credence to the other aspects of the fit to the $\xi = 0.03$–0.04 data. Finally, we note that although there is a strong correlation between the values of α'' and b, the best fit is obtained when both are non-zero.

The fit leads to definite predictions for the s-dependence of $\frac{d^2\sigma}{d\xi dt}$ at fixed ξ and t, as discussed in the previous section. The solid curves in Figs. 26 and 27 are calculated using the quoted convergence values of the free parameters and, not unexpectedly, in Fig. 26 passes through the UA8 point at $-t = 1.0$ GeV^2 and the averages of the ISR points at $-t = 1.0$ and 0.20 GeV^2 which were used in the fit. However, because the CDF points points are are outside our fitted range of s and, in particular, $-t = 0.05$ GeV^2 is below our fitted range of t, it is remarkable that they are in reasonable agreement with the solid curves.

The dashed curves are Eq. 4, evaluated following the prescription of Goulianos[29] (see Sect. 4.2). As discussed above, they do not agree with the data. If the renormalization hypothesis alone is discarded, then the prediction follows the linear segment of the dashed curve over the entire range of s shown in the figure, in disagreement with the data. It is thus clear that the one-component $\sigma_{\mathcal{P}p}^{total}$ hypothesis must also be incorrect. If the renormalization hypothesis is retained, then $\sigma_{\mathcal{P}p}^{total}$ would have to increase much more rapidly with s than it does.

We now turn to the larger ξ-region, 0.03–0.09, where non-$\mathcal{P}$omeron-exchange background must be included. This background is described by adding an empirical background term[43] to Eq. 4 of the form:

$$\left(\frac{d^2\sigma}{d\xi dt}\right)_{Background} = A\xi^1 e^{ct}, \tag{11}$$

with different values of A and c for the ISR data and the UA8 data. In all fits described below where data in the larger ξ-range, 0.03–0.09, are used, the background term is applicable.

We have also attempted to describe the background by adding other Reggeon terms in the triple-Regge formula, but could not achieve acceptable fits. This is perhaps not surprising, since we know that there are other types of background. For example, it is known that 10% of all protons at $\xi = 0.1$ come from large-x_p production of Δ^{++}[44]. There can also be other types of experiment-dependent backgrounds.

Table 7 shows the results of all simultaneous fits made to the UA8 and ISR data[15] in the larger ξ-range, 0.03–0.09. Fit "A" is the fit to the $\xi = 0.03$–0.04 data, described above. Fit "B" adds to these data all the UA8 data up to $\xi = 0.09$. Fit "C" does the same as Fit "B" except that the ISR data and not the UA8 data are added. Fit "D" adds both to the $\xi = 0.03$–0.04 data.

Although, when comparing Fits "B" and "C", we see some evidence of systematic shifts of the parameters, the errors do tend to overlap in the two cases. Of more significance is the fact that the results from Fit "D" are seen to agree rather well with Fit "A". In particular, $K\sigma_0$, α'', b and R in the two cases are consistent within the quoted statistical uncertainties. The fact that the two fits yield self-consistent results is a good indication that they are reliable. We believe that Fit "D" is the best available description of the experimental differential cross section, $\frac{d^2\sigma}{d\xi dt}$.

It is particularly interesting to note that the value $R = 4.0 \pm 0.6$, is comparable to the ~3.5 value found in the fits to real $pp/p\bar{p}$ total cross sections[37, 38]. This seems to say that the relative strengths of $\mathcal{P}$omeron and a/f_2-exchange are nearly the same in proton-proton and $\mathcal{P}$omeron-proton total cross sections.

Figures 29, 30, 31, 32 and 33 display most of the data used in the fits described in this section. Superimposed on the data points are the fitted curves (using Fit "D") for signal plus background and background alone. The curves are seen to be in reasonably good agreement with the data used.

5.5 One-pion-exchange

Since one-pion-exchange (OPE) is a well-established phenomenon, we consider to what extent it can account for the non-$\mathcal{P}$omeron-exchange background found in our fits. The exchanged particle in the diagram of Fig. 3 would then be a π^0.

At high energies, large s' and low $|t|$, the Chew-Low equation[45] can be written in terms of a "π^0 flux factor in the proton[46], $F_{\pi^0/p}(t, \xi)$ (i.e., for a single-arm in pp-collisions):

$$\frac{d^2\sigma}{d\xi dt} = F_{\pi^0/p}(t, \xi) \cdot \sigma_{\pi^0 p}(s') \tag{12}$$

$$F_{\pi^0/p}(t, \xi) = \frac{14.6}{4\pi} \frac{|t|}{(t - \mu^2)^2} \xi^1 [F_{ope}(t)]^2$$

where, as in Eq. 4 for the $\mathcal{P}$omeron, the squared mass at the upper vertex, $s' = \xi s$ (ξ is now the pion's momentum fraction in the proton). The factor, 14.6, is the π^0-nucleon

coupling constant at the lower vertex in Fig. 3 with an exchanged pion, μ is the pion mass and $\sigma_{\pi^0 p}(s')$ is the π^0-proton total cross section ($\sim$ 29 mb). In contrast with the $\sim \xi^{-1}$ dependence for the $\mathcal{P}$omeron, the ξ^1 dependence for the pion reflects the fact that $\alpha_\pi(t) \sim 0$ at low $|t|$ (and that the pion contains a beam-proton valence quark).

$F_{ope}(t)$ is an empirical form factor which was shown in the early days of OPE studies, 30 years ago, to extrapolate correctly to on-shell cross sections at the pion-exchange pole in the scattering amplitude. Its form is given in Ref. [47].

Using Eq. 12 and the form factor from Ref. [47], the dotted curve at $-t = 0.15$ in Fig. 31 shows the expected OPE contribution to the observed cross section. We see that the OPE background is only a small part of the total non-$\mathcal{P}$omeron-exchange background.

5.6 Breakdown of the triple-Regge formula in the resonance region

It is interesting to investigate how low in s' and s the triple-Regge formula describes data. To determine this, we note that, in the absence of non-$\mathcal{P}$omeron-exchange background, Eq. 7 at fixed t can be rewritten as:

$$(s)^{1-2\alpha(t)} \cdot \frac{d^2\sigma}{d\xi dt} \propto (s')^{1-2\alpha(t)} \cdot \sigma_{\mathcal{P}p}^{total}(s') \tag{13}$$

Thus, a plot of the differential cross section multiplied by $s^{1-2\alpha(t)}$ vs. s' should be independent of s.

Figures 34(a-d) show this quantity from three fixed-target experiments at Fermilab[25, 27, 26], plotted vs. s' ($s' = \xi s$) in 4 different t-bins; only data with $s' > 3$ GeV^2 and $\xi < 0.03$ are plotted, in order to avoid resolution smearing on the low side, and background contributions on the high side. In each case, there are data at several different s-values.

We may draw the following conclusions from Figs. 34. There appears to be pronounced resonance structure, whose t-dependence is steeper than for the general $\mathcal{P}$omeron-exchange signal. There are striking dependences on s, mainly at the lowest $|t|$-values, thus limiting the validity of Eq. 4 for s' values less than about 12 GeV^2 and for s below about 400 GeV^2.

6 Longitudinal structure in diffraction

Longitudinal energy-flow along the beam direction ("beam-jets") is a well-established property of high energy hadronic interactions. One of the dominant features of diffractive interactions that has come to light in recent years is that the outgoing particle distributions in the diffractive center-of-mass (X system) are also p_t-limited and far from the isotropic shape expected from the old "fireball" model of diffraction. Since "beam jets" tend to contain spectator-like partons from the beam particles, one may speculate that the observation and study of such jets in diffractive systems might eventually lead to further understanding of the partonic structure of the $\mathcal{P}$omeron.

Early evidence for p_t-limited distributions in diffraction is found in Refs. [48, 49, 50, 51]. Experiment R608 at the CERN Intersecting Storage Rings studied several exclusive diffractive final states from React. 1 and found that the final-state X systems possess sharp longitudinal structures[52, 53, 24] in their centers-of-mass. The UA4 Collaboration[54], using measured track pseudorapidity distributions at $\sqrt{s} = 546$ GeV, also presented evidence against the "fireball" model of diffractive systems.

One of the most striking examples of longitudinal structure is in the following reaction from the R608 experiment[52, 53]:

$$p\,p \rightarrow (\Lambda^\circ \overline{\Lambda}^\circ p)\,p, \tag{14}$$

where $(\Lambda^\circ \overline{\Lambda}^\circ \mathrm{p})$ is the X system and all three particles are seen in the final state. In the X center-of-mass, a forward (backward) Λ° is always correlated with a backward (forward) proton. The particles both have average momenta, normalized to $\sqrt{s'}/2$, of $|0.6|$. For both cases, the $\overline{\Lambda}^\circ$ is at rest (its average momentum is 0.0).

Figure 35 shows the diagrams which correspond to the reported effect. In each case the exchanged $\mathcal{P}$omeron appears to interact with a single quark in the incident proton and to "kick" it backwards, thereby stretching the color string between quark and diquark. The observed baryon pair production in this final state requires that both a diquark pair and a quark pair be produced. Depending on their relative spatial ordering, the lambda (proton) is forward or backward (backward or forward). In either case the $\overline{\Lambda}^\circ$ remains essentially at rest in the X system. The R608 results were interpreted as evidence for $\mathcal{P}$omeron-single quark interactions[53].

In Refs. [52, 53], data on the final state $p \rightarrow \Lambda^\circ \phi K^+$ are also presented. In that case, two $s\overline{s}$ quark pairs come from the stretched string, the Λ° usually goes forward and the ϕ remains at rest in the X system.

Experiment R608 also studied the reaction: $p \rightarrow \Lambda^\circ K^+$ [55, 56]. Not only are the Λ° and K$^+$ sharply peaked forward and backward, respectively, but the Λ° is observed to have a very large polarization, over 60%. This remarkably large polarization is due in large part to the absence of dilution effects from Σ^* and Σ° decay background.

Because the $\sqrt{s'}$ values in the reactions studied in R608 were rather small (e.g. 3 GeV), compared with the enormously larger values in the present UA8 experiment, we may expect that the details of the $\mathcal{P}$omeron-proton interaction will be quite different.

6.1   Energy-flow

With the use of the calorimeter information associated with each event in our data sample of React. 1, we look for evidence of longitudinal structure in the inclusive flow of energy in the center-of-mass of the diffractive system. Since, for the events studied here, the calorimeter was not used in the trigger, its offline use allows for an unbiased study of the X-system in the events.

We define an energy-flow quantity, $dE_{CM}/d(cos\theta_{CM})$, where E_{CM} and θ_{CM} are the energy and polar angle of a particular UA2 calorimeter cell, in the diffractive center-of-

mass. This quantity has the advantage that isotropy in the energy-flow would appear as a flat distribution in $cos\theta_{CM}$.

In order to obtain $dE_{CM}/d(cos\theta_{CM})$ we note that, at fixed s', each UA2 θ–cell boundary transforms to a unique $\theta_{\rm CM}$ value. Thus the total energy in each laboratory θ-bin in the UA2 calorimeter can be transformed to a corresponding θ_{CM}-bin in the X center-of-mass. Figure 36 shows the range of $\theta_{\rm CM}$ "seen" by the UA2 calorimeter system as a function of diffractive mass. The motion of the X center-of-mass is responsible for the forward-backward asymmetry in the acceptance in this system and for the fact that, for diffractive masses larger than about 40 GeV, we have almost perfect acceptance in the $\mathcal{P}$omeron hemisphere.

Table 8 contains the average values (per event) of $dE_{CM}/d(cos\theta_{CM})$ vs. θ_{CM} for $\sqrt{s'}$ values of 50, 130 and 190 GeV, respectively. Figures 37(a-c) show these values plotted vs. θ_{CM}. It is clear that the energy-flow in the center-of-mass of diffractive systems is highly anisotropic and that there is a sharp peak along the $\mathcal{P}$omeron axis, which may be interpreted as a $\mathcal{P}$omeron "beam jet" in the $\mathcal{P}$omeron-proton interaction. The essential shape for $\sqrt{s'} < 200$ GeV is observed to be independent of s', (and also of whether or not jets are present in the final state — not shown here). From the results in Fig. 37, coupled with the R608 results, we may infer that a similar sharp peak also exists in the proton direction.

7   Conclusions

We have presented the results of a measurement of the differential cross section for the single-diffractive reactions: $p_i + \bar{p} \rightarrow p_f + X$ and $p + \bar{p}_i \rightarrow X + \bar{p}_f$ at $\sqrt{s} = 630$ GeV, in the momentum transfer range, $0.8 < -t < 2.0$ GeV^2 and final state Feynman-$x_p > 0.90$.

Double differential cross sections are compared with previous measurements at the ISR and S$p\bar{p}$S-Colliders. Despite the order of magnitude increase in center of mass energy and the large differences in total cross sections, we find only a small difference in diffractive cross sections from lower energy measurements.

Several new features of the $\mathcal{P}$omeron Flux Factor are determined from simultaneous fits to these UA8 data and similar data from the CHLM collaboration at the CERN-ISR. Prominent among these is that the $\mathcal{P}$omeron Regge trajectory requires a term quadratic in t, with coefficient, $\alpha'' = 0.079 \pm 0.012$ GeV^{-4}, which may indicate the onset of the hard $\mathcal{P}$omeron, or a contribution from multiple $\mathcal{P}$omeron-exchange.

We also show that existing data require a $\mathcal{P}$omeron-proton cross section that decreases at small mass and increases at large mass, similar to other reactive total cross sections. We have obtained the parameter, $K\sigma_0 = 0.72 \pm 0.10$ mb/GeV^2, where K is the unknown normalization constant of the $\mathcal{P}$omeron Flux Factor in the proton and σ_0 is the constant in the $\mathcal{P}$omeron-proton total cross section at high energies, $\sigma_0(s')^\epsilon$. The data are inconsistent with the s-dependent K proposed by Goulianos.

Finally, we used the UA2 calorimetry to investigate the energy-flow in the diffractive final state. A striking longitudinal structure is observed in the final state which supplies

further evidence that the $\mathcal{P}$omeron undergoes a hard interaction with one or more partons of the target particle.

8 Acknowledgements

References

[1] For reviews, see e.g.:

    K. Goulianos, Phys. Reports 101 (1983) 169;
    G. Alberi and G. Goggi, Phys. Reports 74 (1981) 1;
    A.B. Kaidalov, Phys. Reports 50 (1979) 157;
    U. Amaldi, M. Jacob and G. Matthiae, Ann. Rev. Nucl. Sci. 26 (1976) 385.

[2] S. Erhan et al. [R603 Collaboration] Phys. Letters B85 (1979) 447.

[3] W. Lockman et al. [R603 Collaboration]; see also, W. Lockman, thesis, University of California, Los Angeles (1978).

[4] G. Ingelman and P.E. Schlein, Phys. Letters B152 (1985) 256.

[5] R. Bonino et al. [UA8 Collaboration], Phys. Letters B211 (1988) 239.

[6] A. Brandt et al. [UA8 Collaboration], Phys. Letters B297 (1992) 417.

[7] A. Brandt et al. [UA8 Collaboration], Phys. Letters B421 (1998) 395.

[8] M. Derrick et al. [ZEUS Collaboration], Phys. Letters B315 (1993) 481; B332 (1994) 228; B338 (1994) 483; B356 (1995) 129; Zeit. Phys. C68 (1995) 569.

[9] T. Ahmed et al. [H1 Collaboration], Nucl. Phys. B429 (1994) 477; Phys. Letters B348 (1995) 681.

[10] F. Abe et al. [CDF Collaboration], Phys. Rev. Letters 79 (1997) 2636.

[11] A. Brandt [DØ Collaboration], Proceedings of the 11th Topical Workshop on Proton-Antiproton Collider Physics, Abano Terme, Italy (1996).

[12] A. Donnachie and P.V. Landshoff, Nucl. Phys. B244 (1984) 322.

[13] A. Brandt et al. [UA8 Collaboration], Nucl. Instrum. & Methods A327 (1993) 412.

[14] C. N. Booth [UA2 Collaboration], Proceedings of the 6th Topical Workshop on Proton-Antiproton Collider Physics (Aachen 1986), eds. K. Eggert et al. (World Scientific, Singapore, 1987) p. 381; A. Beer et al., Nucl. Instrum. & Methods 224 (1984) 360.

[15] M.G. Albrow et al., Nucl. Phys. B54 (1973) 6;
    M.G. Albrow et al., Nucl. Phys. B72 (1974) 376.

[16] R. Battiston et al. [UA4 Collaboration], Nucl. Instrum. & Methods A238 (1985) 35.

[17] M. Bozzo et al. [UA4 Collaboration], Phys. Letters B136 (1984) 217.

[18] D. Bernard et al. [UA4 Collaboration], Phys. Letters B186 (1987) 227.

[19] J. G. Zweizig et al. [UA8 Collaboration], Nucl. Instrum. & Methods A263 (1988) 188.

[20] A. Brandt et al. [UA8 Collaboration], "Measurements of inclusive $\bar{\Lambda}$ production with large x_Λ at the S$p\bar{p}$S-Collider", submitted to Nucl. Phys. B (1997).

[21] A. Brandt et al. [UA8 Collaboration], to be published (1998);
N. Ozdes, Ph.D. Thesis (Cukurova University - Adana, Turkey - 1992);
"Observation of Double $\mathcal{P}$omeron Exchange Reaction at the S$p\bar{p}$S-Collider", contribution to Singapore Conference (2–8 August, 1990).

[22] J. Alitti et al. [UA2 Collaboration], Phys. Letters B257 (1991) 232; see also UA2 $p\bar{p}$ Note 580.

[23] A. Kuzucu, Ph.D. Thesis (Cukurova University - Adana, Turkey - 1992).

[24] A.M. Smith et al. [R608 Collaboration], Phys. Letters B167 (1986) 248.

[25] R.D. Schamberger et al., Phys. Rev D17 (1978) 1268.

[26] R.L. Cool et al., Phys. Rev. Letters 47 (1981) 701.

[27] Y. Akimov et al., Phys. Rev. Letters 39 (1977) 1432.

[28] F. Abe et al. [CDF Collaboration], Phys. Rev. D50 (1994) 5535.

[29] K. Goulianos, Phys. Letters B358 (1995) 379; B363 (1995) 268.

[30] M.G. Albrow et al., Nucl. Phys. B108 (1976) 1.

[31] J.C.M. Armitage et al., Nucl. Phys. B194 (1982) 365.

[32] N.A. Amos et al. [E710 Collaboration], Phys. Letters B301 (1993) 313.

[33] A.H. Mueller, Phys. Rev. D2 (1970) 2963; D4 (1971) 150.

[34] R.D. Field and G.C. Fox, Nucl. Phys. B80 (1974) 367.

[35] A. Donnachie and P.V. Landshoff, Nucl. Phys. B231 (1984) 189; Nucl. Phys. B267 (1986) 690.

[36] A. Donnachie and P.V. Landshoff, Phys. Letters B296 (1992) 227.

[37] J.R. Cudell, K. Kyungsik and K.K. Sung, Phys. Letters B395 (1997) 311;
J.R. Cudell, K. Kang and S.K. Kim, "Simple Model for Total Cross Sections", preprint, Brown-HET-1060, January 1997.

[38] R.J.M. Covolan, J. Montanha and K. Goulianos, Phys. Letters B389 (1996) 176.

[39] L. Frankfurt and M. Strikman, Phys. Rev. Letters 63, (1989) 1914; 64 (1990) 815.

[40] J.C. Collins, L. Frankfurt and M. Strikman, Phys. Letters B307 (1993) 161.

[41] A.B. Kaidalov, L.A. Ponomarev and K.A. Ter-Martirosyan, Sov. J. Nucl. Phys. 44 (1986) 468.

[42] A. Capella, A. Kaidalov, C. Merino and J. Tran Thanh Van, Phys. Letters B337 (1994) 358.

[43] For example, see: J.C. Sens, Proceedings of 14th Scottish Universities Summer School in Physics (Academic Press - 1974, ed. R.L. Crawford and R. Jennings) 105 and : M.G. Albrow et al., Nucl. Phys. B108 (1976) 1, and references therein.

[44] F.T. Dao et al., Phys. Letters B45 (1973) 399.

[45] G.F. Chew and F.E. Low, Phys. Rev. 113 (1959) 1640.

[46] P.E. Schlein, Phys. Letters B332 (1994) 136.

[47] Z. Ming Ma et al., Phys. Rev. Letters 23 (1969) 342.

[48] M.G. Albrow et al., Nucl. Phys. B102 (1976) 275.

[49] D. Aston et al., Nucl. Phys. B166 (1980) 1.

[50] D. Aston et al., Nucl. Phys. B189 (1981) 15.

[51] M. Atkinson et al., Nucl. Phys. B229 (1983) 269.

[52] J. Alitti and S. Erhan, Diffractive Production of $\mathbf{\Lambda^\circ \phi^\circ K^+}$ and $\mathbf{\Lambda^\circ \overline{\Lambda}^\circ p}$ in proton-proton interactions at the ISR, Proceedings of the First International Workshop on Elastic and Diffractive Scattering, Blois, France (3–6 June, 1985) Editions Frontieres (ed. B. Nicolescu and J. Tran Thanh Van), p. 121.

[53] A.M. Smith et al. [R608 Collaboration], Phys. Letters B163 (1985) 267.

[54] D. Bernard et al. [UA4 Collaboration], Phys. Letters B166 (1986) 459.

[55] S. Erhan et al. [R608 Collaboration], Observation of Polarization in Diffractive Dissociation $\mathbf{p \rightarrow \Lambda^\circ K^+}$ at the CERN-ISR. Proceedings of XV Symposium Multiparticle Dynamics (Lund-1984), p. 62.

[56] T. Henkes et al. [R608 Collaboration], Phys. Letters B283 (1992) 155.

Selection Cuts	Remaining Fraction
Triggers	1.0
One Track with $x_p > 0.9$	0.59
No Hit in Adjacent Spectrometer	0.58
Pileup	0.52
Halo	0.45
Energy Topology (see text)	0.42

Table 1: Effect of offline cleanup cuts on the initial triggered data sample of 150K events. The fraction of the initial data sample which remains after each cut is shown. The final combined data sample for both Roman-pot positions (12σ and 14σ, respectively, from the beam orbit) is 62,627 events. The YN and NN events (see text) are rejected in the final "event topology" cut. See the text for explanations of the various cuts.

Trigger Component or Offline Cut	Efficiency
Trigger Processor: chamber hit logic	0.902
Trigger Processor: momentum calculation	0.974
Scintillation Veto: halo	0.995
Scintillation Veto: adjacent arm	0.998
Off-line Cut: pileup (average)	0.908
Off-line Cut: halo	0.916
Net Efficiency (not including geometric acceptance)	0.726

Table 2: The various Trigger and Cut Efficiencies used in cross section calculations. The geometric acceptance is not included in this table.

	$-t$				(GeV^2)		
	0.95	1.05	1.15	1.30	1.50	1.70	1.90
ξ							
0.09	0.77±0.08	0.65±0.08	0.38±0.06	0.26±0.02	0.14±0.02	0.11±0.02	0.05±0.02
0.08	0.79±0.07	0.53±0.06	0.43±0.06	0.24±0.02	0.16±0.02	0.13±0.02	0.06±0.02
0.07	0.66±0.07	0.44±0.06	0.43±0.06	0.30±0.02	0.17±0.02	0.09±0.02	0.04±0.02
0.06	0.65±0.07	0.58±0.07	0.49±0.06	0.23±0.02	0.17±0.02	0.11±0.02	0.10±0.02
0.05	0.70±0.07	0.50±0.06	0.42±0.06	0.27±0.02	0.16±0.02	0.11±0.02	0.08±0.02
0.04	0.81±0.07	0.60±0.07	0.48±0.06	0.29±0.02	0.17±0.02	0.14±0.02	0.09±0.02
0.03	0.99±0.08	0.59±0.06	0.45±0.06	0.37±0.03	0.20±0.02	0.16±0.02	0.08±0.02

Table 3: Single Diffractive Differential Cross Sections: $\frac{d^2\sigma}{d\xi dt}$ (mb/GeV^2). The cross sections are single arm and correspond to $p\bar{p} \to p + X$ OR $p\bar{p} \to \bar{p} + X$. The errors shown are statistical only. Not included is a 10–15 % systematic uncertainty in the absolute cross section. See text for a discussion of the uncertainty in the t-values.

$-t$ (GeV^2)	$d\sigma/dt$ (mb/GeV^2)
0.85	0.2060 ± 0.0036
0.95	0.1520 ± 0.0031
1.05	0.1040 ± 0.0016
1.15	0.0855 ± 0.0015
1.25	0.0608 ± 0.0013
1.35	0.0437 ± 0.0011
1.45	0.0339 ± 0.0010
1.55	0.0261 ± 0.0009
1.65	0.0218 ± 0.0009
1.75	0.0168 ± 0.0008
1.85	0.0135 ± 0.0007
1.95	0.0092 ± 0.0006

Table 4: Single Diffractive Differential Cross Sections: $d\sigma/dt$ (mb/GeV^2) for $x_p > 0.95$. The cross sections are single arm and correspond to $p\bar{p} \to p + X$ OR $p\bar{p} \to \bar{p} + X$ (single arm). The points are plotted in Fig. 19. The integral for the $|t|$ region, 1–2 GeV^2, is 41.5 μb.

$-t$ bin	χ^2	χ^2/D.F.	$\alpha(t)$ 1-comp.	χ^2	χ^2/D.F.	$\alpha(t)$ 2-component
1.0–1.1	19.0	2.7	1.01 ± 0.01	17.0	2.4	0.94 ± 0.01
1.1–1.2	15.5	2.2	0.98 ± 0.01	14.3	2.0	0.91 ± 0.01
1.2–1.4	2.4	0.3	0.98 ± 0.01	6.5	0.9	0.92 ± 0.01
1.4–1.6	3.1	0.4	0.93 ± 0.01	6.9	1.0	0.89 ± 0.01

Table 5: Fit results for the $\mathcal{P}$omeron Regge trajectory in four bins of t, from 1.0–1.6 GeV^2. In each case results are given for two types of fits, the first assuming 1-component in $\sigma^{total}_{\mathcal{P}p}$ and the second assuming 2-components in $\sigma^{total}_{\mathcal{P}p}$. In each case, the χ^2 and the χ^2 per degree of freedom are given.

χ^2	χ^2/DF	$K\sigma_0$ (mb GeV^{-2})	α'' (GeV^{-4})	b (GeV^{-2})	R
413	8.8	0.68 ± 0.02	–	–	–
391	8.5	0.86 ± 0.05	-0.029 ± 0.006	–	–
331	7.2	1.28 ± 0.08	–	0.62 ± 0.06	–
199	4.4	2.32 ± 0.15	0.156 ± 0.011	2.4 ± 0.2	–
108	2.3	0.51 ± 0.02	–	–	5.2 ± 0.4
98	2.2	0.40 ± 0.03	–	-0.20 ± 0.06	6.3 ± 0.6
85	1.9	0.41 ± 0.03	0.020 ± 0.004	–	6.4 ± 0.5
65	1.5	0.67 ± 0.08	0.078 ± 0.013	0.88 ± 0.19	5.0 ± 0.6

Table 6: Fit results of Eqs. 4 and 5 to experimental values of $\frac{d^2\sigma}{d\xi dt}$ (mb/GeV^2) in the ξ-range, 0.03–0.04. There are 48 data points in all fits.

	Fit "A"	Fit "B"	Fit "C"	Fit "D"
χ^2	65	117	357	393
Data	48	84	257	292
χ^2/DF	1.5	1.5	1.4	1.4
$K\sigma_0$ (mb GeV^{-2})	0.67 ± 0.08	0.53 ± 0.14	0.81 ± 0.13	0.72 ± 0.10
α'' (GeV^{-4})	0.078 ± 0.013	0.055 ± 0.012	0.074 ± 0.014	0.079 ± 0.012
b (GeV^{-2})	0.88 ± 0.19	0.66 ± 0.18	0.95 ± 0.24	1.08 ± 0.20
R	5.0 ± 0.6	6.8 ± 0.7	2.8 ± 0.5	4.0 ± 0.6
A(ua8)	–	23 ± 8	–	25 ± 7
A(551)	–	–	296 ± 40	280 ± 30
A(930)	–	–	232 ± 26	226 ± 21
c(ua8) (GeV^{-2})	–	2.2 ± 0.2	–	2.1 ± 0.2
c(isr) (GeV^{-2})	–	–	3.5 ± 0.2	3.5 ± 0.1

Table 7: Fit results of Eqs. 4 and 5 to experimental values of $\frac{d^2\sigma}{d\xi dt}$ (mb/GeV^2). Fit "A" is to both UA8 and ISR data in the ξ-range, 0.03–0.04. Fits "B", "C" and "D" add the indicated UA8 and/or ISR data in the ξ-range, 0.04–0.09, to the Fit "A" sample, and include background in the fit of the form, $A\xi^1 e^{ct}$, as discussed in the text.

$\sqrt{s'}= 50$ GeV		$\sqrt{s'}= 130$ GeV		$\sqrt{s'}= 190$ GeV	
$cos(\theta_{CM})$	$\frac{dE_{CM}}{dcos(\theta_{CM})}$	$cos(\theta_{CM})$	$\frac{dE_{CM}}{dcos(\theta_{CM})}$	$cos(\theta_{CM})$	$\frac{dE_{CM}}{dcos(\theta_{CM})}$
-0.211	1.04±0.02	-0.815	7.88±0.16	-0.909	23.05±0.50
-0.179	1.36±0.02	-0.640	4.57±0.09	-0.814	11.36±0.25
-0.407	1.30±0.02	-0.473	2.44±0.06	-0.714	5.34±0.14
0.558	1.44±0.03	-0.307	1.58±0.04	-0.603	2.86±0.09
0.680	2.06±0.04	-0.118	1.48±0.04	-0.461	2.12±0.06
0.774	3.69±0.07	0.080	1.78±0.05	-0.291	2.09±0.06
0.842	5.98±0.12	0.271	1.91±0.05	-0.101	1.93±0.06
0.890	10.8±0.3	0.440	2.63±0.08	0.092	2.22±0.07
0.927	22.5±0.4	0.597	4.48±0.09	0.300	2.90±0.07
0.954	33±1	0.725	5.83±0.14	0.493	3.17±0.09
0.969	49±1	0.808	7.96±0.22	0.631	3.92±0.11
0.979	70±2	0.864	12.3±0.4	0.730	5.57±0.18
0.985	102±3	0.903	18.9±0.6	0.803	7.41±0.25
0.989	152±5	0.931	29.8±0.9	0.857	11.4±0.4
0.993	209±7	0.951	50.1±1.5	0.898	18.7±0.7
0.995	375±11	0.966	87.4±2.5	0.929	34.2±1.0
0.997	495±16	0.977	161 ±4	0.952	62.2±1.7
0.998	724±24	0.985	330 ±8	0.969	124±3
0.9986	930±53	0.991	487 ±17	0.980	182±7
0.9991	1260±60	0.994	885 ±25	0.986	318±10
0.9994	1450±90	0.996	1400±40	0.991	530±17
0.9996	1540±120	0.997	1720±60	0.994	745±24
0.9997	4650±250	0.9980	2730±100	0.996	1230±40
0.9998	2160±220	0.9987	5530±180	0.997	2550±70
0.9999	2190±260	0.9992	9230±240	0.998	5820±130
0.99995	3190±420	0.9996	12900±410	0.999	11230±250

Table 8: The average Energy-Flow per event (GeV) in the center-of-mass of the X System in React. 1: $dE_{CM}/dcos(\theta_{CM})$ for three different values of $\sqrt{s'}$. In each case, the 26 entries correspond to the 26 θ-cells of the UA2 calorimeter (8 in each end-cap plus 10 in the central calorimeter). The θ_{CM} values are quoted at the center of each cell.
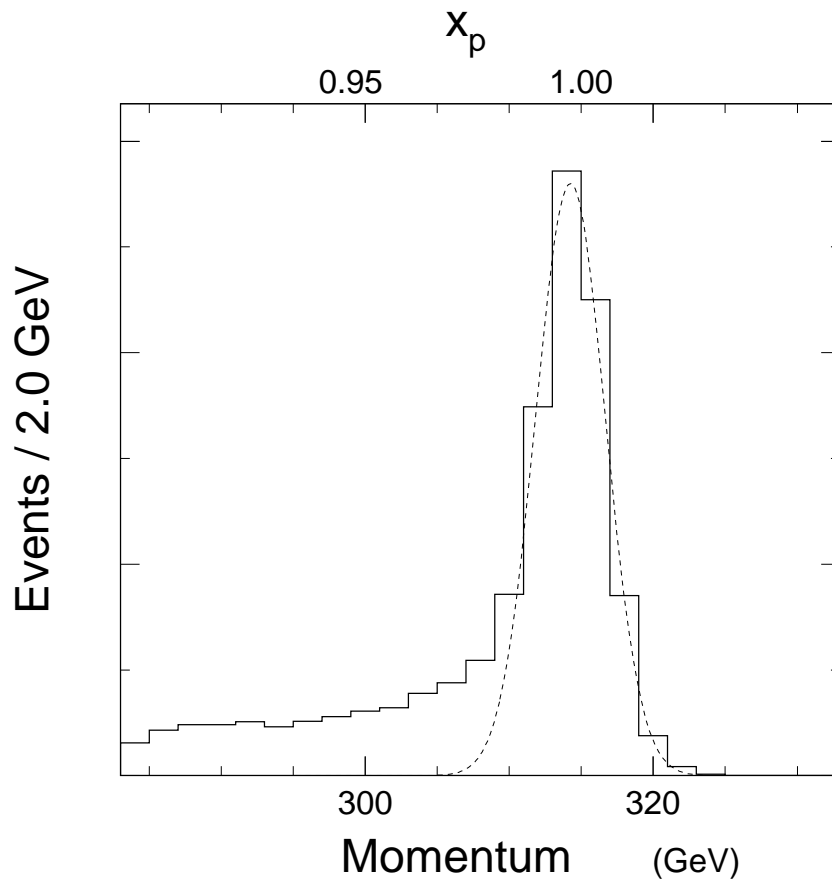
Figure 1: A raw $\bar{p}$ momentum distribution measured in this experiment, summed over all t. The dashed curve is a Gaussian resolution which mirrors the high side of the distribution, and shows that the resolution smearing of the peak is mainly confined to x_p values larger than about 0.97.
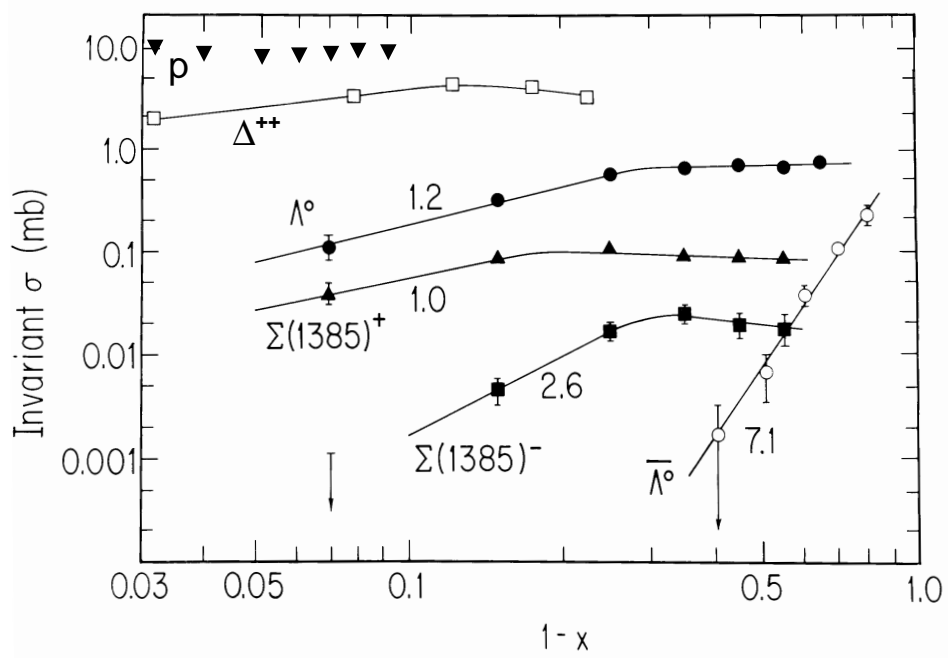
Figure 2: Invariant cross sections for (inclusive) forward baryons[2] in proton-proton inter-actions at the CERN Intersecting Storage Rings, integrated over transverse momentum, $(x/\pi)d\sigma/dx$ vs. $\xi = 1 - x$. σ includes a factor of 2, to account for production in both hemispheres. Δ^{++} points are from Ref. [3]. The proton points are estimates from UA8. The numbers labeling each set of data points is the exponent of the straight line $(1 - x)^n$
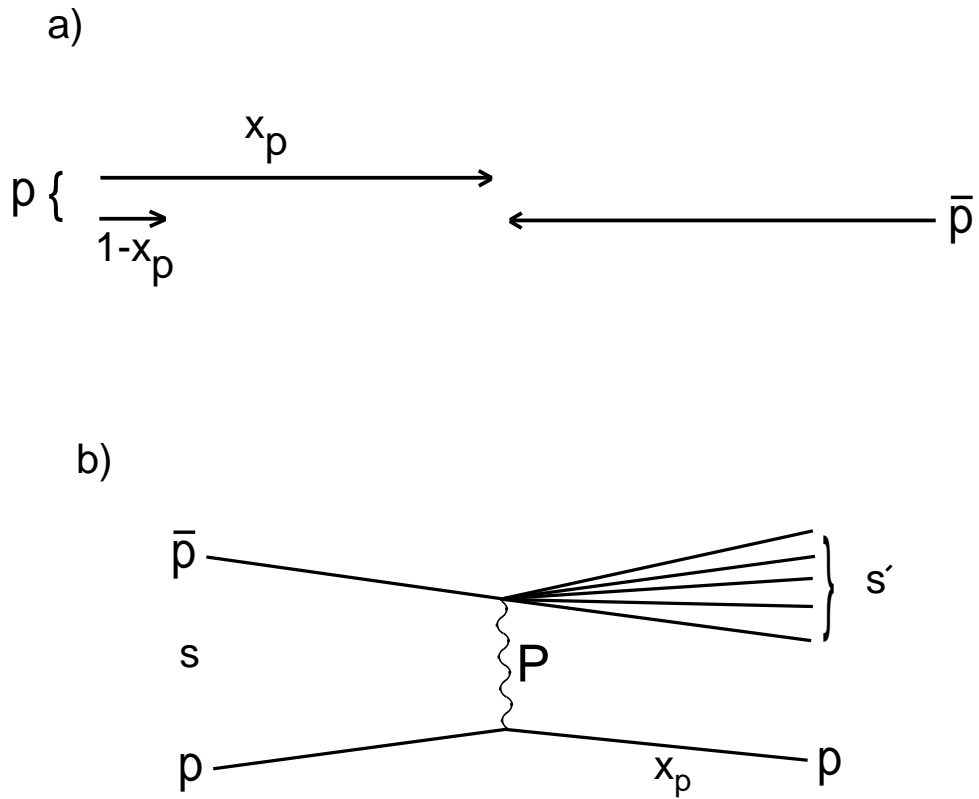
Figure 3: (a) Incident $\mathcal{P}$omeron with beam momentum fraction $\xi = 1 - x_p$ interacts with the incident $\bar{p}$. (b) Characteristic t-channel diagram for diffractive processes in which a $\mathcal{P}$omeron is exchanged. s and s' are kinematically related by: $s' = (1 - x_p)s = \xi s$. The observed spectator proton has Feynman-x_p.
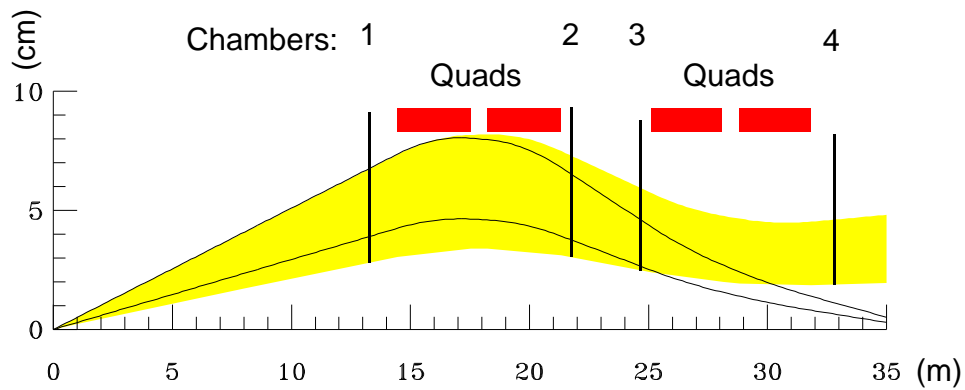
Figure 4: Particle trajectories through a Roman-pot spectrometer. The labels, "Quads", refer to the low-β machine quadrupole magnets. The center of the UA2 detector is at $z = 0$ at the left side of the sketch. The vertical lines indicate the positions of the UA8 wire chambers in the Roman-pots. The solid curves show the trajectories of 300 GeV particles ($x_p \sim 0.95$) emerging from the center of the intersection region with minimum and maximum acceptable angles. The lower (upper) edge of the shaded area corresponds to the minimum (maximum) angle of an elastic track which is accepted. The trajectory corresponding to the lower edge of the shaded region in this sketch is 12 beam widths (σ) from the center of the circulating beam orbit.
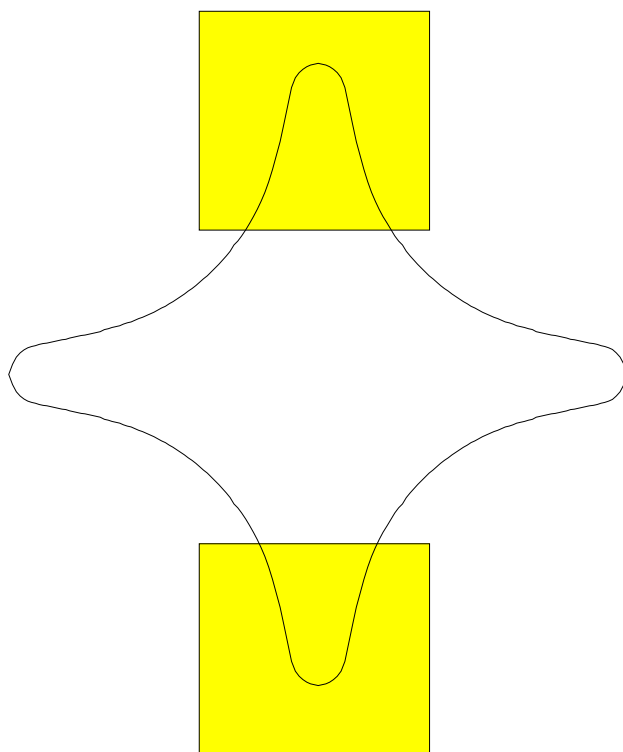
Figure 5: The UA8 spectrometer aperture viewed from the interaction region. The shaded rectangles indicate the sensitive regions of the first wire chambers at a distance $z = 13$ m from the interaction region center. The curved line indicates the walls of the beam pipe inside the quadrupole magnets.
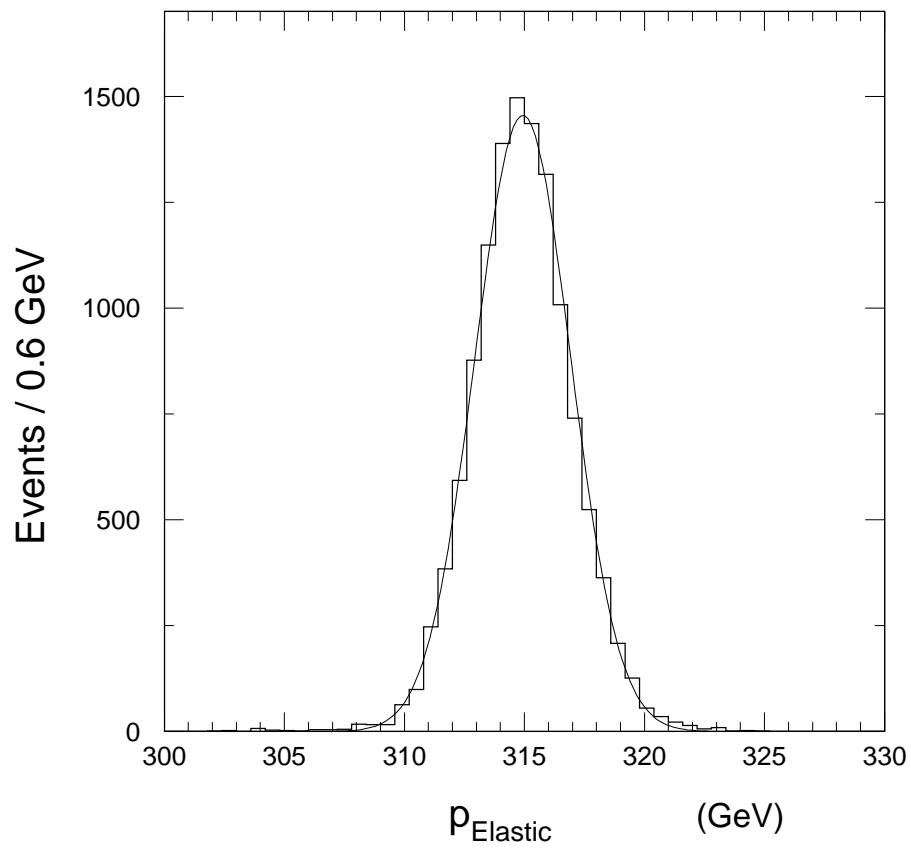
Figure 6: An elastic momentum spectrum measured by UA8. The curve is a Gaussian fit to the data histogram and has a width, $\sigma_p/p = 0.0061$.
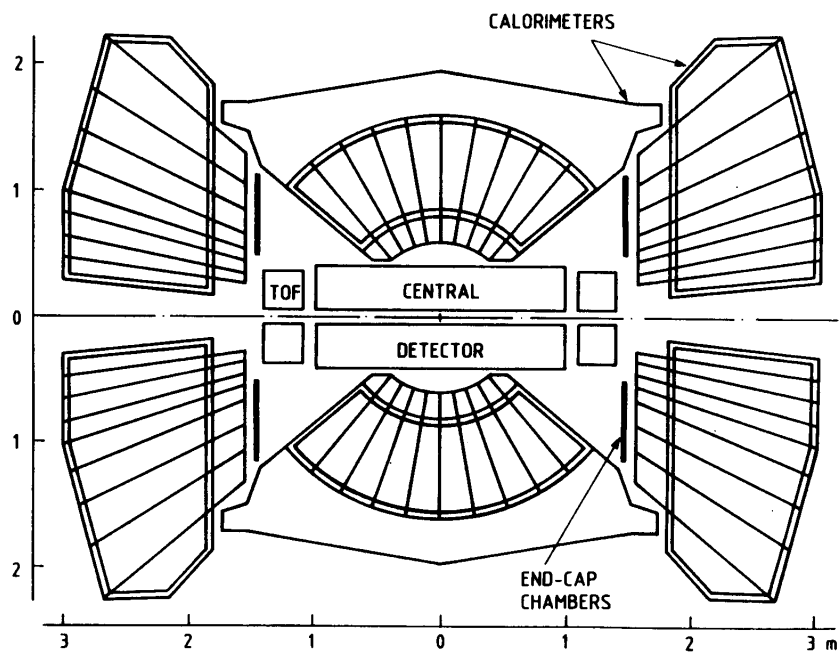
Figure 7: A cross sectional view of the upgraded UA2 apparatus. Detectors which were important for the analysis described here are the Calorimeters, the Time-of-Flight counters (TOF) and the Silicon Vertex Detector within the Central Detector assembly. The TOF counters covered the pseudorapidity range, 2.3 to 4.1 in each arm.
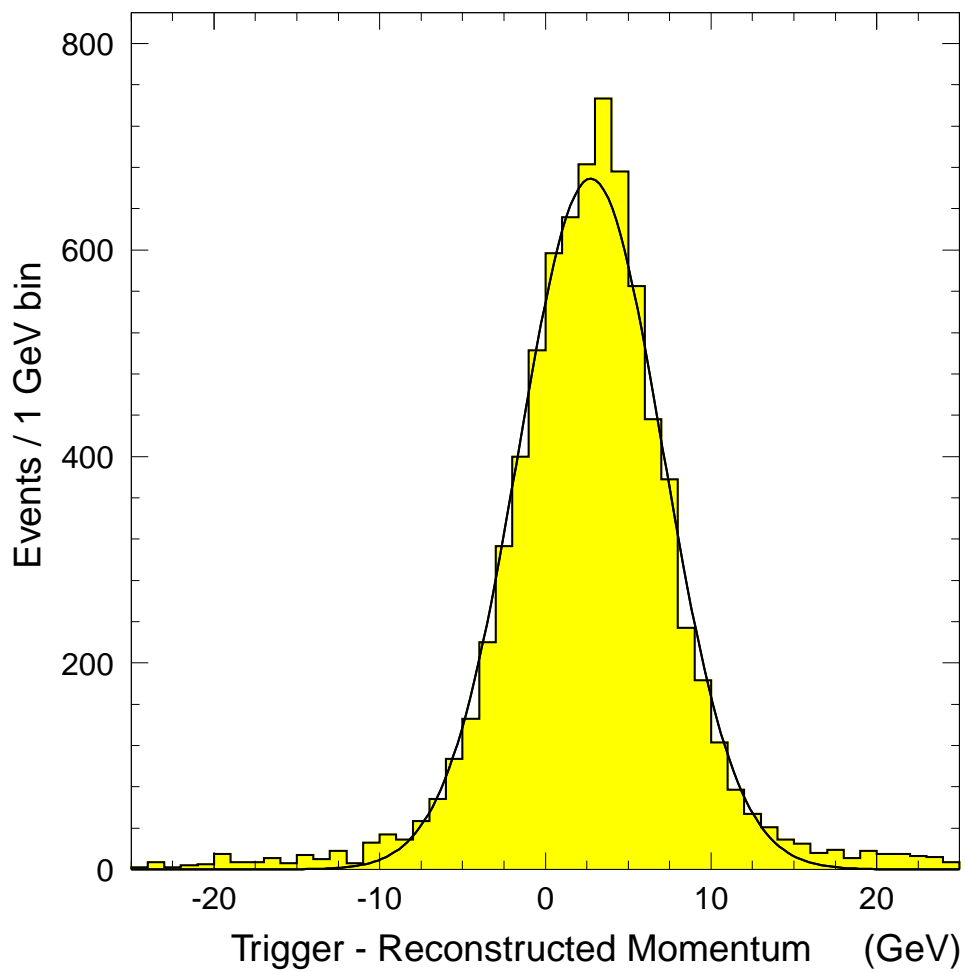
Figure 8: The difference between momentum calculations made by the trigger processor and in the offline analysis. The curve is a Gaussian fit with $\sigma = 4.4$ GeV. The offset of the mean value from zero is discussed in the text.
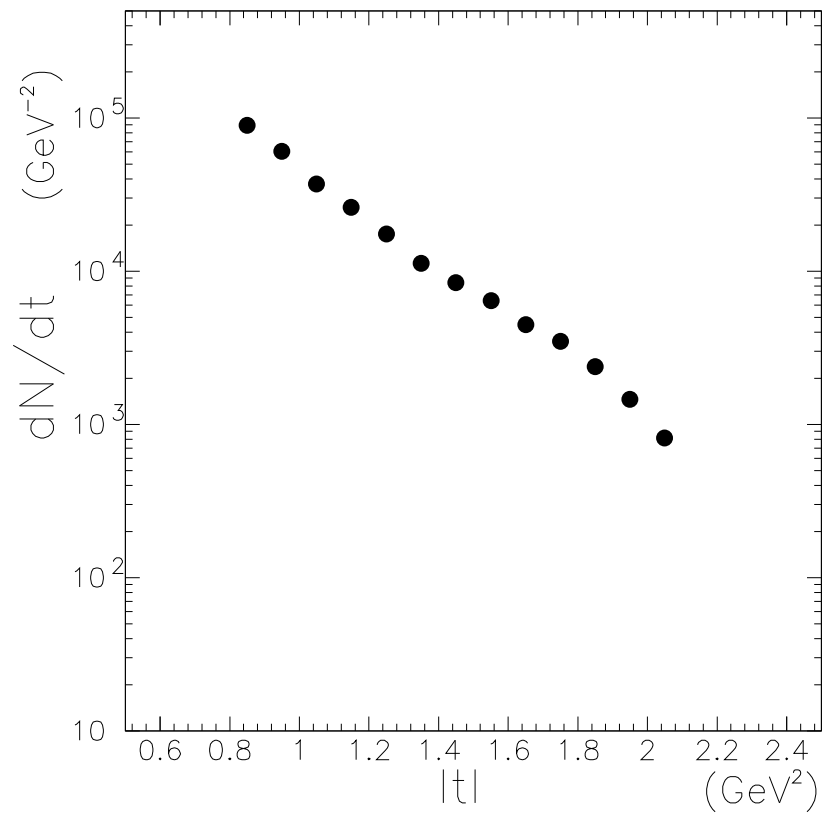
Figure 9: Raw (uncorrected) momentum transfer (t) distribution of events with an antiproton in the upper $\bar{p}$ spectrometer. The plot contains both 14σ and 12σ data.
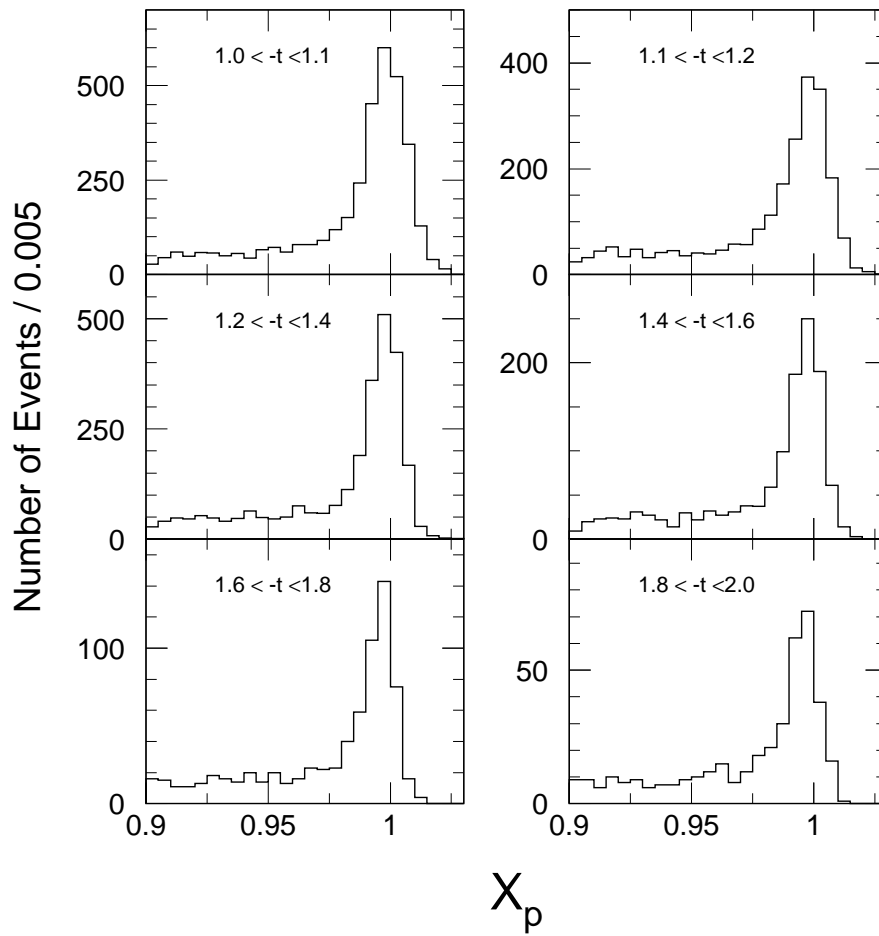
Figure 10: Uncorrected $x_p = 1 - \xi$ distributions in the indicated t-bins, where t is given in units of GeV^2.
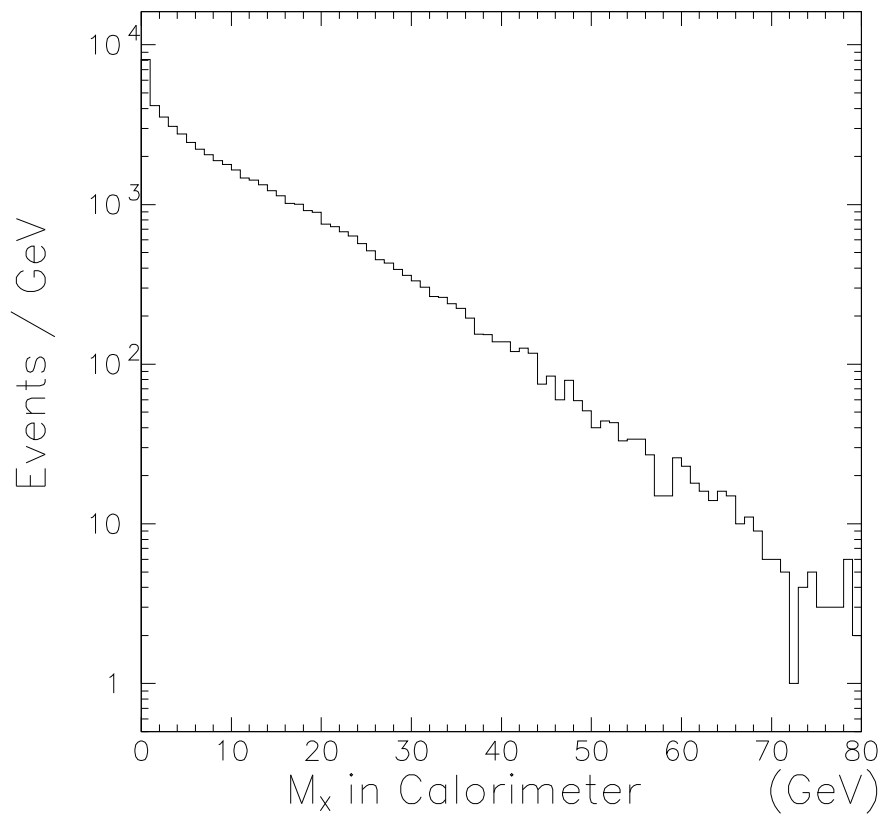
Figure 11: The uncorrected total invariant mass seen by the UA2 calorimeter for events with $x_p > 0.9$.
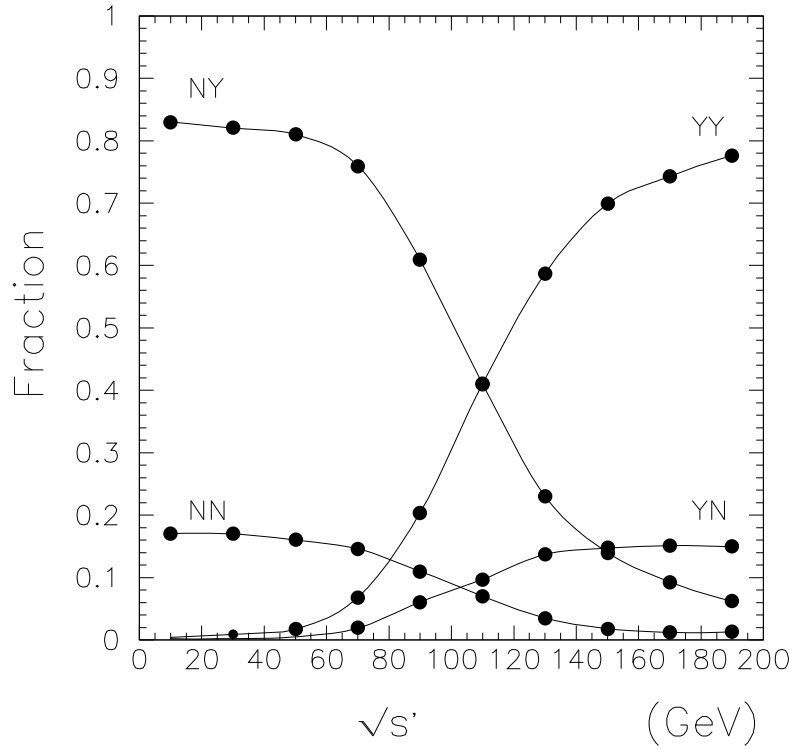
Figure 12: Dependence on diffractive mass of the four different TOF-counter hit topologies. The curves show the relative frequencies of events with no TOF counter hits (NN), hits only opposite the detected p or $\bar{p}$ (NY), hits only on the same side as the detected p or $\bar{p}$ (YN) and hits in both sides (YY), respectively. The experimental mass resolution, $\sigma(\sqrt{s'}) = 1230/\sqrt{s'}$ GeV, results in some "smearing" of the NY and NN curves at low mass.
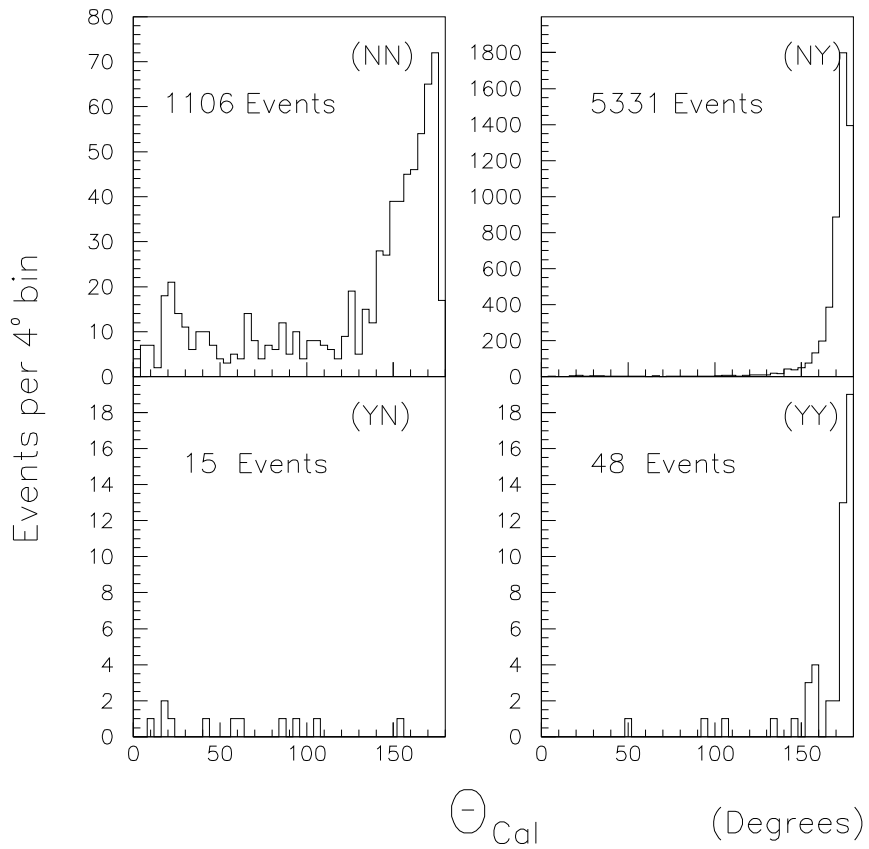
Figure 13: Angular distributions of the calorimeter-energy-sum vector for the four TOF topologies, selected for low-mass at the center of the diffractive peak ($x_p \sim 1$). As in Fig. 12, the labels refer to the TOF counters which have hits (e.g., NY means "No" for counters on the same side as the detected proton and "Yes" for counters on the opposite side). Note that, in the NN (NY) plots, 443 (230) of the 1106 (5331) events do not appear in the histogram, because there is no energy deposited in the calorimeter. The trigger side is at $0°$.
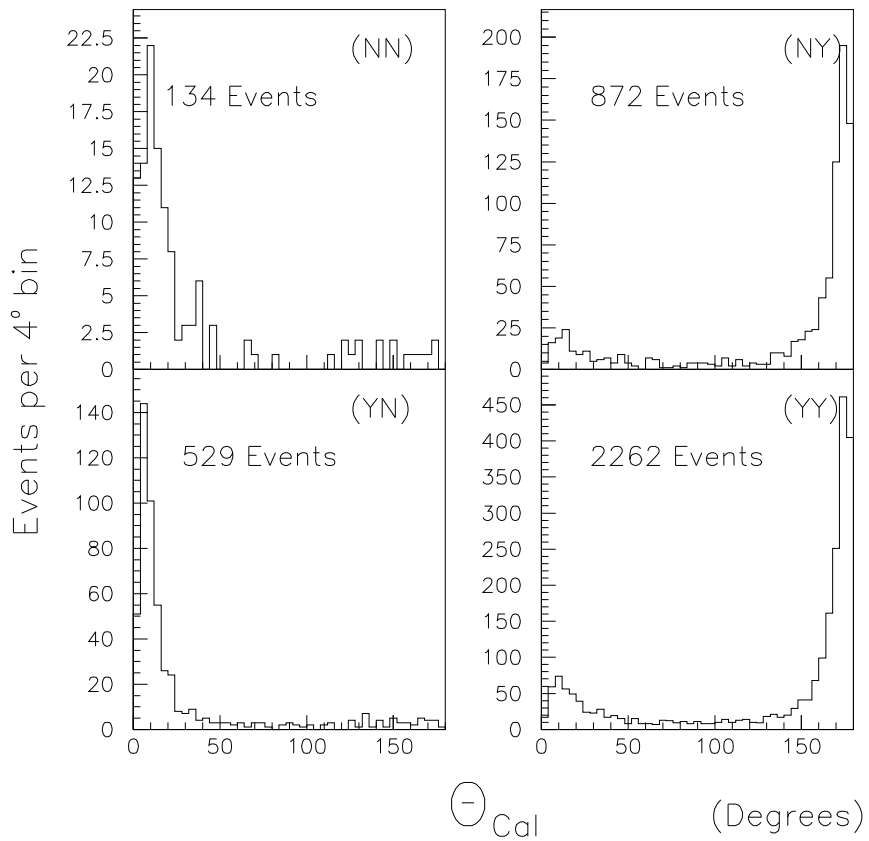
Figure 14: Angular distributions of the calorimeter-energy-sum vector for the four TOF topologies in diffractive events with $\sqrt{s'} = 130$ GeV. As in Fig. 12, the labels refer to the TOF counters which have hits (e.g., NY means "No" for counters on the same side as the detected proton and "Yes" for counters on the opposite side). The trigger side is at 0°.
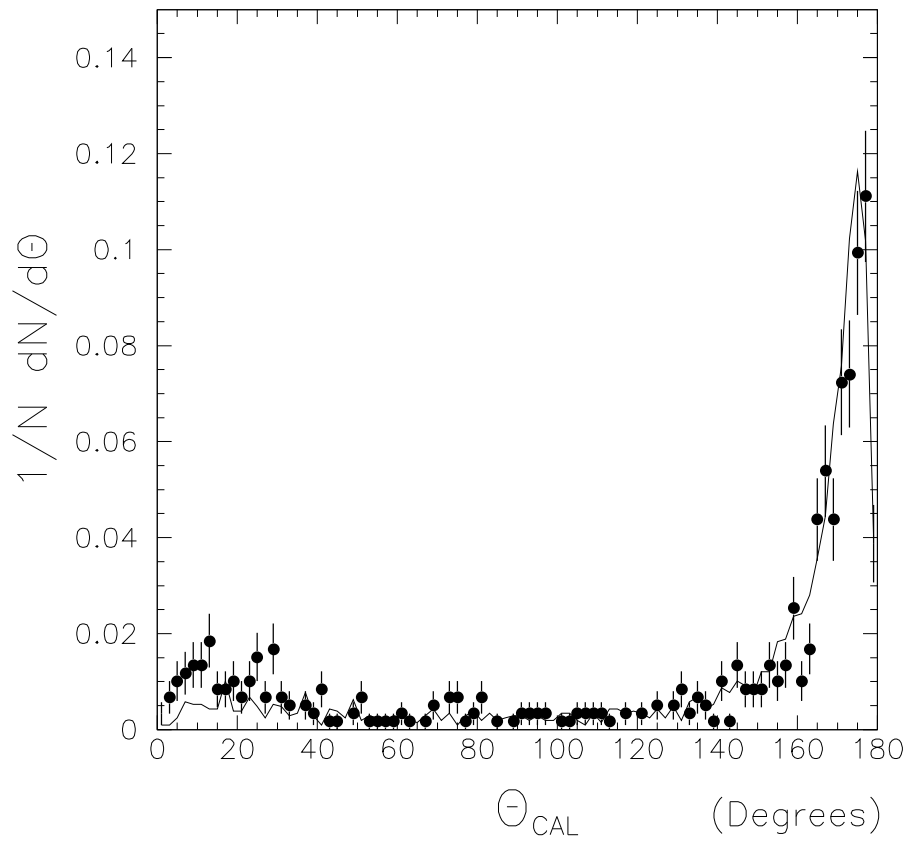
Figure 15: Polar angle of the energy sum vector in the UA2 calorimeter system, θ_{cal}, for NY and YY events with $\sqrt{s'} = 130$ GeV (see Fig. 14) and total transverse calorimeter energy in the range, $5 < \Sigma E_t < 10$ GeV. The curve from the Monte Carlo calculation is normalized to the data.
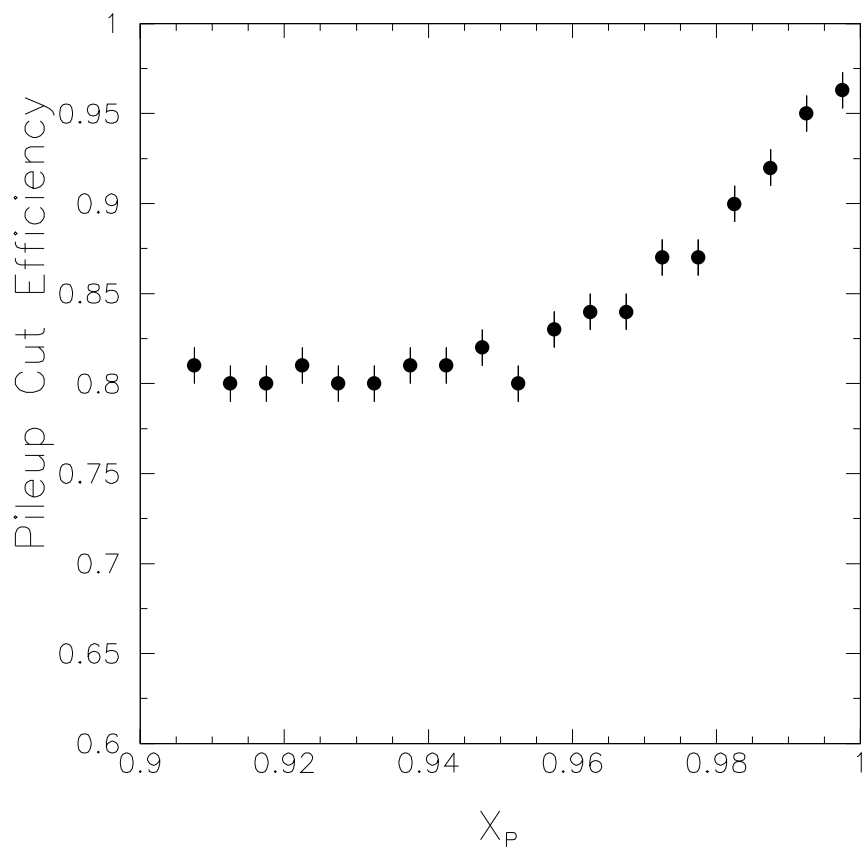
Figure 16: The fraction of good events which survive the pileup cut (see description in text) as a function of the observed track's x_p.
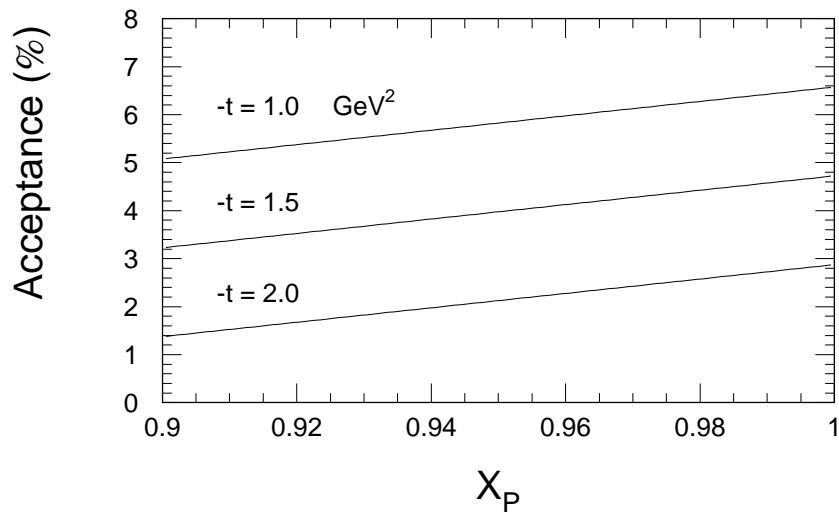
Figure 17: Geometric acceptance of one spectrometer (upper $\bar{p}$) vs. x_p at three values of momentum transfer. This acceptance corrects a single-spectrometer cross section for full ϕ-dependence in its arm. See discussion in text.
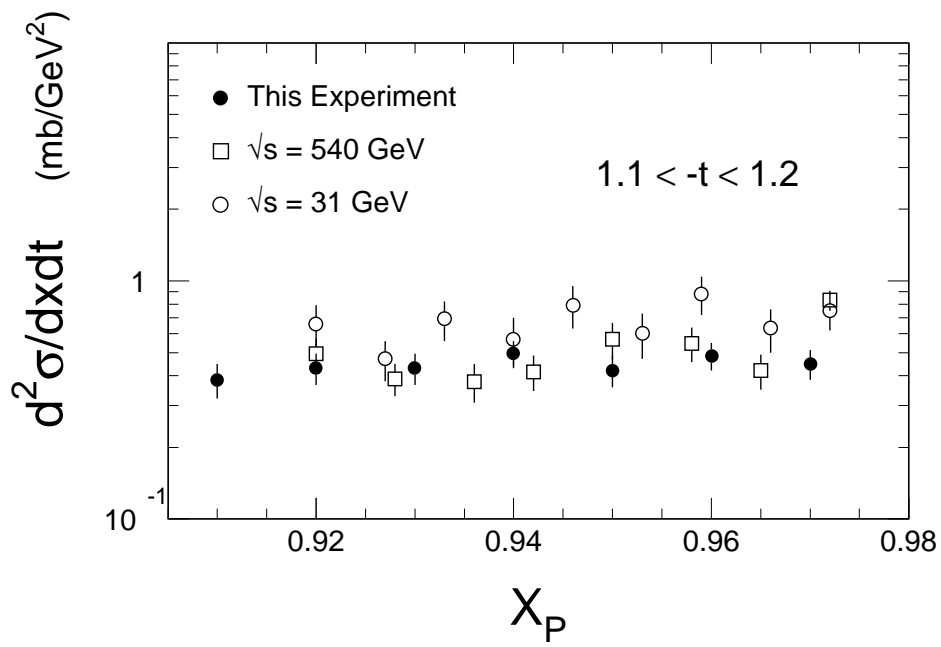
Figure 18: UA8 differential cross section vs. x_p, for the $|t|$-bin, 1.1–1.2 GeV^2, compared with results from Experiment UA4[17] and the ISR[15].
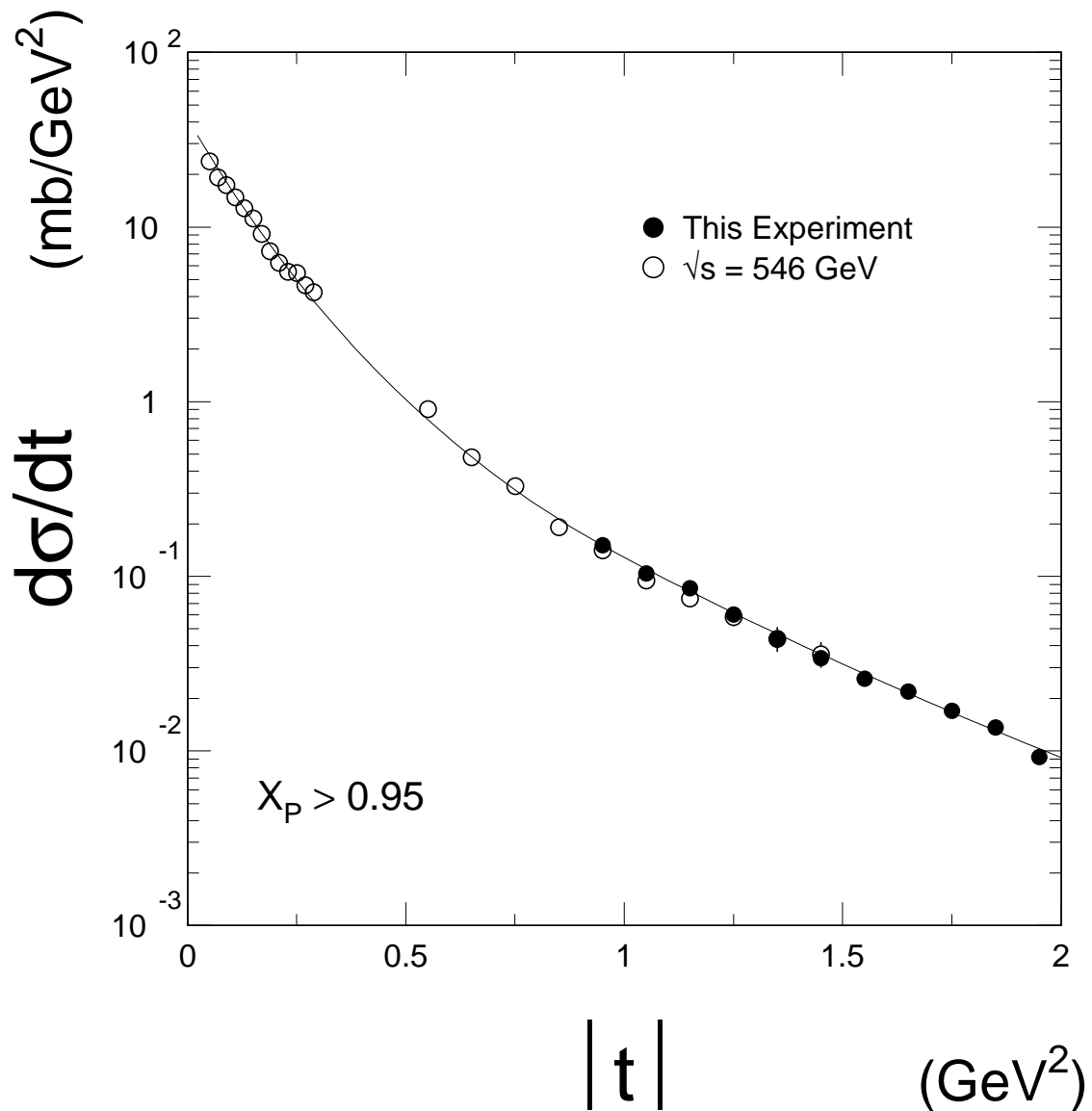
Figure 19: Inclusive differential cross section for protons in React. 1 when $x_p > 0.95$, measured in this experiment and in experiment UA4[17, 18] with $\sqrt{s} = 546$ GeV. As in Table 4, the cross sections shown are for a single arm. Thus, the integral is one-half the total single-diffractive cross section, σ_{sd}^{total}. The curve is to "guide-the-eye".
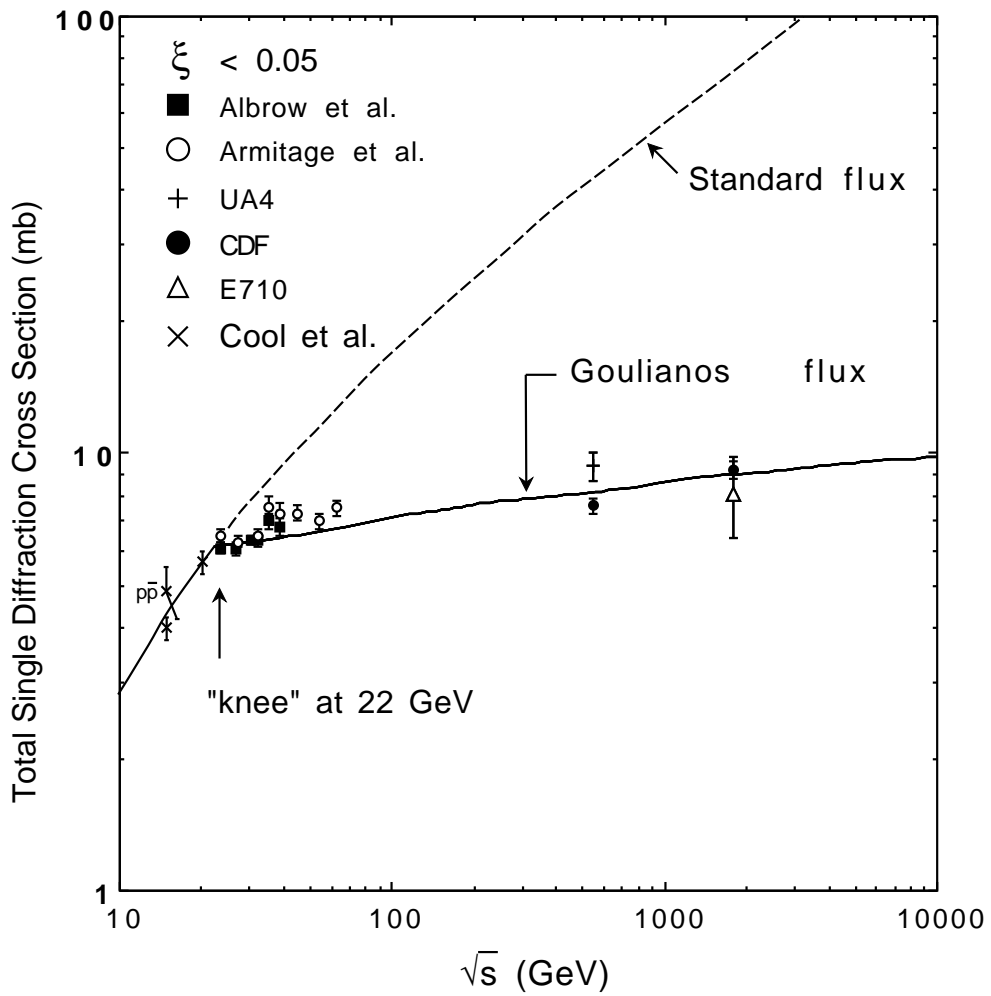
Figure 20: Summary[29] of existing measurements of the total single diffractive cross section (including a factor of 2x for both arms) for $\xi < 0.05$. Dashed curve is the prediction using the standard Triple-Regge flux factor; solid curve is from Goulianos[29].
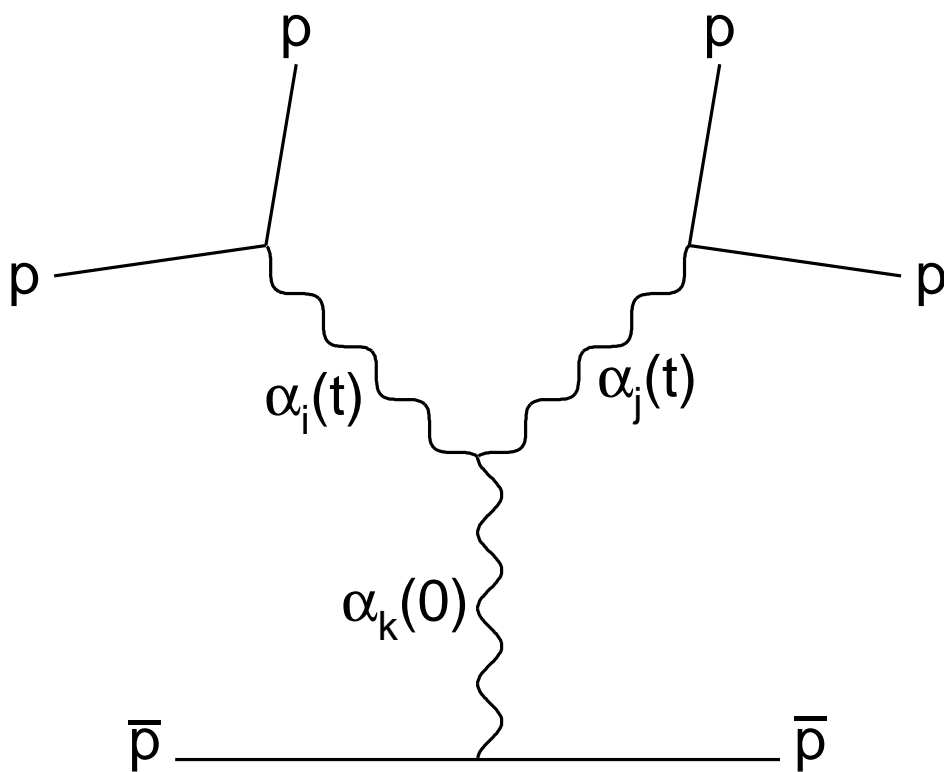
Figure 21: Triple-Reggeon graph.
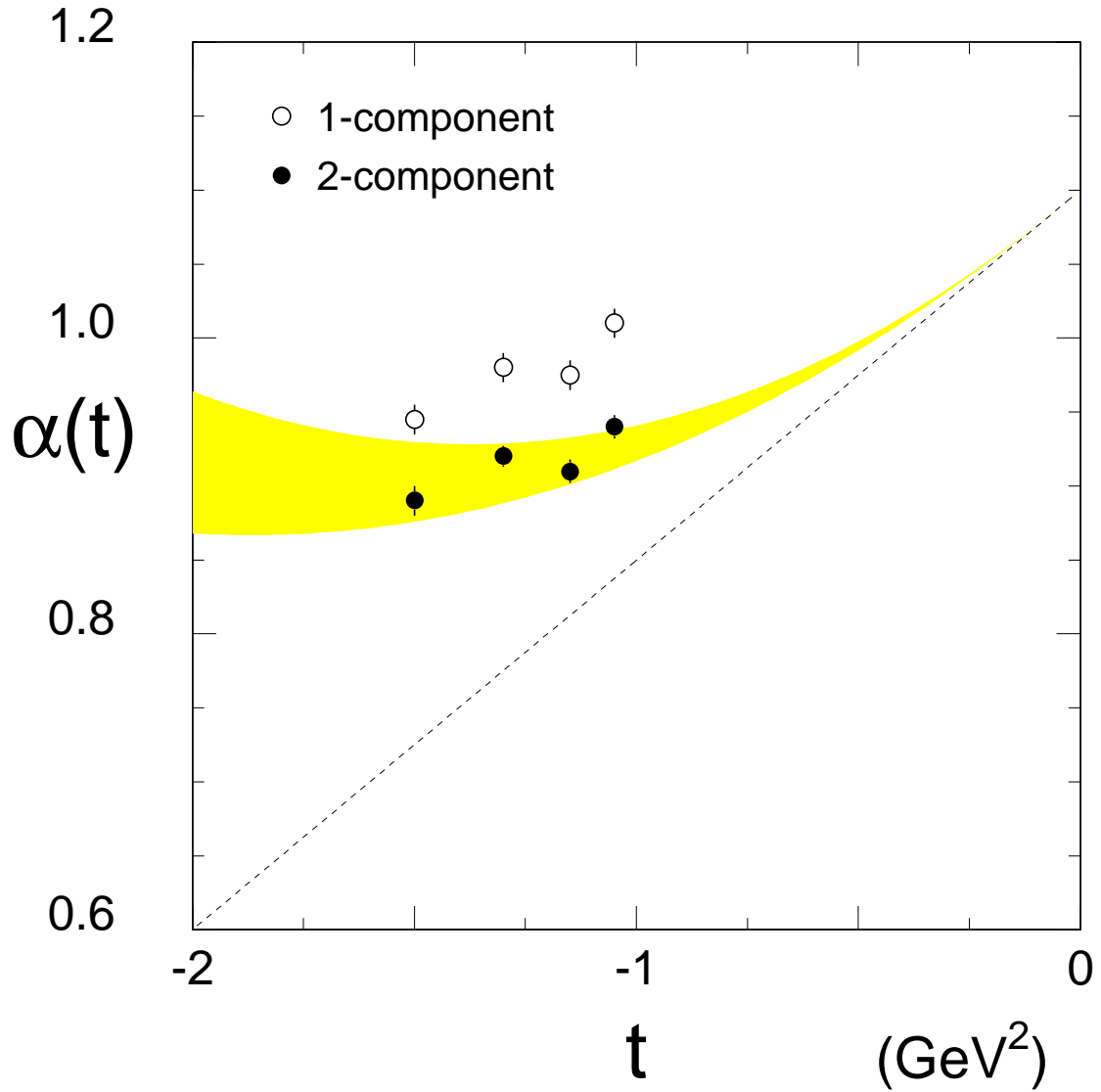
Figure 22: The $\mathcal{P}$omeron $\alpha(t)$ points are from fits to the small-ξ peak regions shown in Fig. 23, as described in the text. The dashed curve is the linear trajectory: $\alpha(t) = 1.10 + 0.25t$. The shaded band shows the effect of adding a quadratic term, $\alpha''t^2 = 0.079t^2$, to the $\mathcal{P}$omeron trajectory in the fits to the data in the ξ-range, 0.03-0.10, described in the text. The width of the shaded band shows the $\pm 1\sigma$ error range on α''.

51
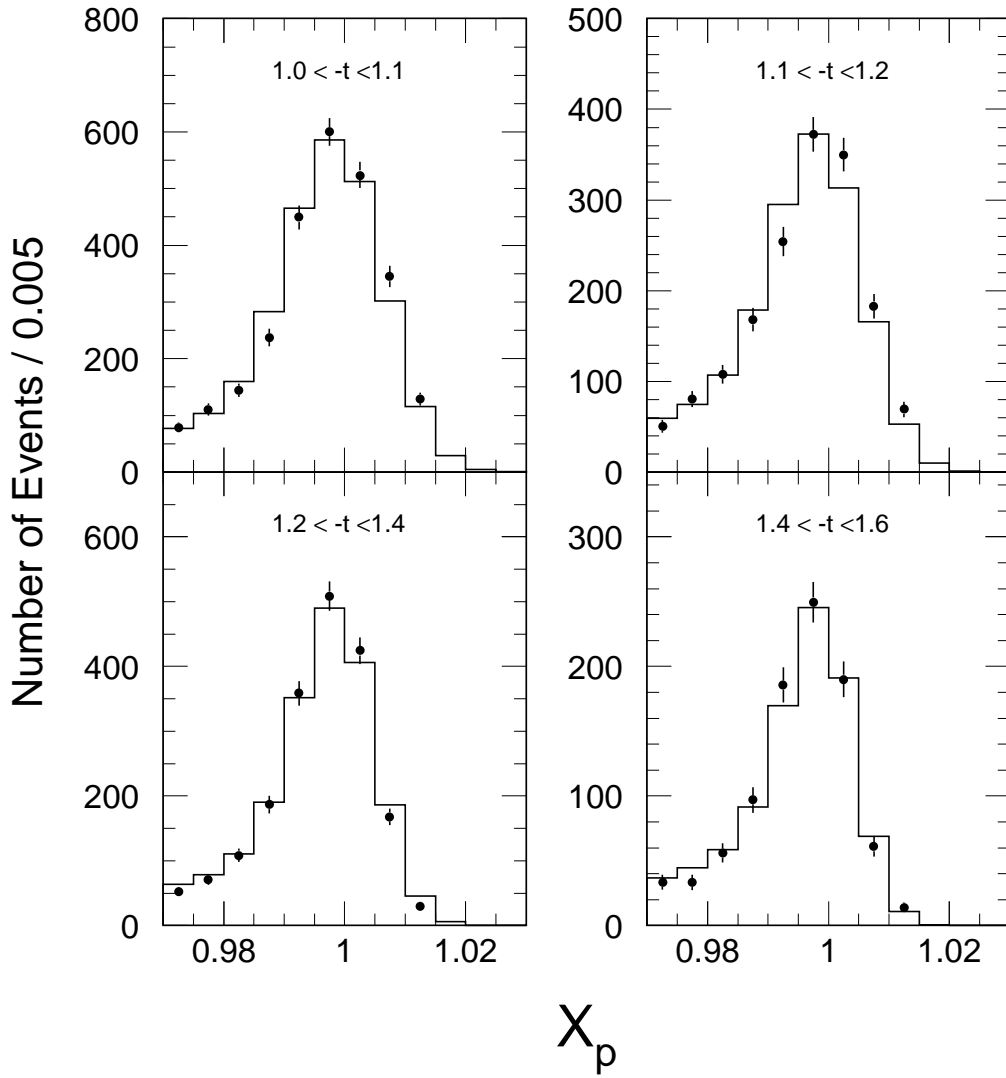
Figure 23: Fits (histograms) of Eq. 8, using both components, to the uncorrected distributions (points) seen in Fig. 10. The inclusion of acceptance and resolution in the fits is described in the text. t is given in units of GeV^2.
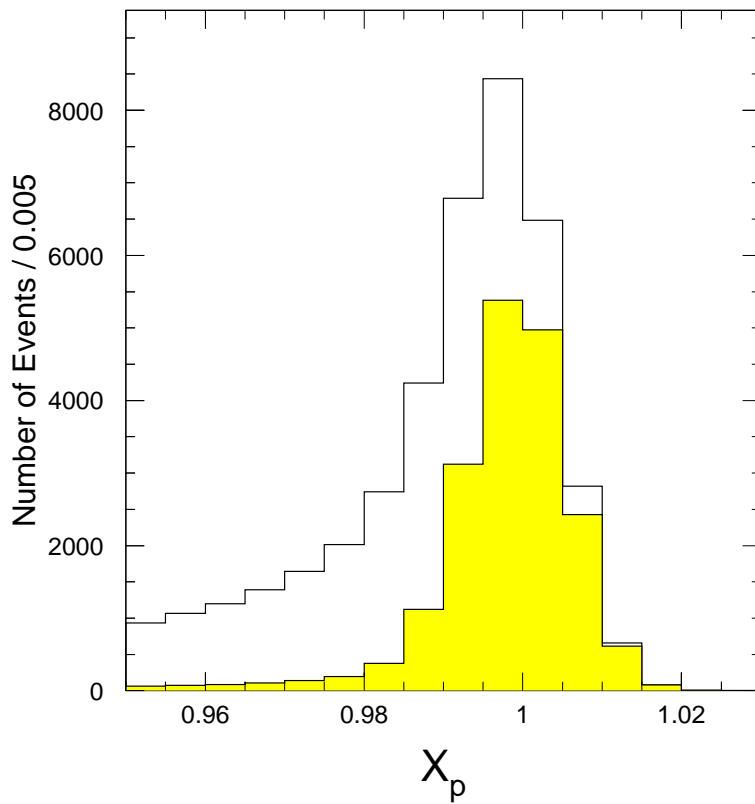
Figure 24: The two terms of Eq. 8 fitted to the data set in Fig. 23 with $1.2 < -t < 1.4$ GeV^2. The $\mathcal{PPP}$ term is open. The shaded distribution superimposed on it is the $\mathcal{PPR}$ term. As discussed in the text, the fits assume $R = 4.0$.
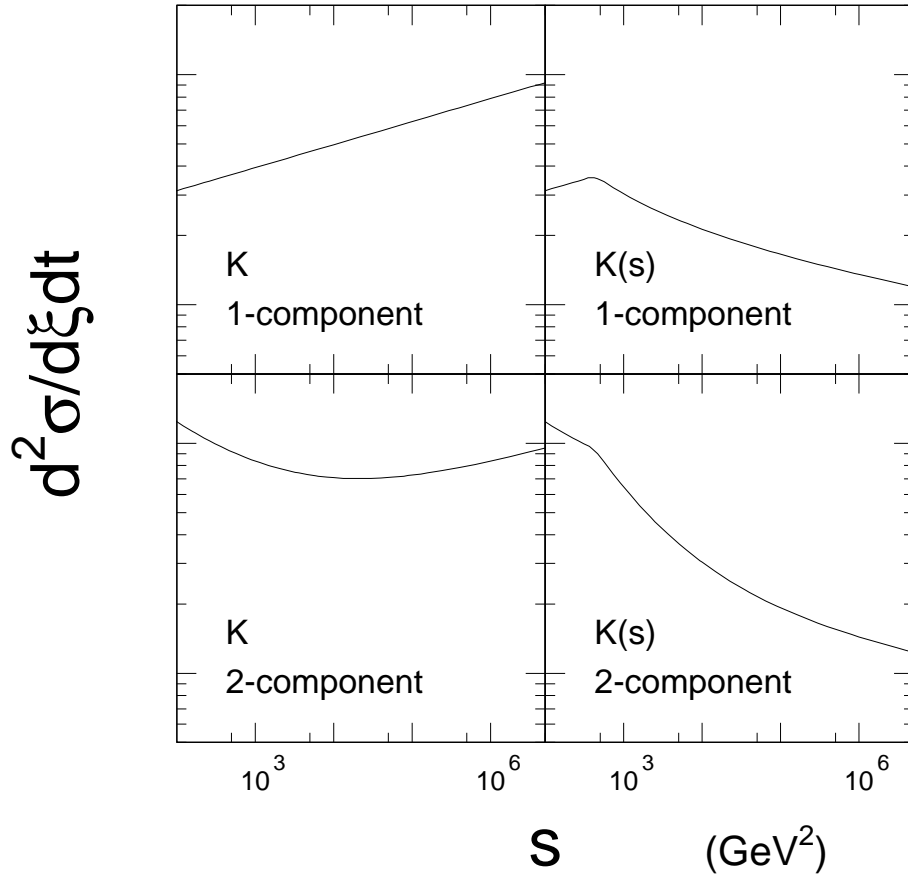
Figure 25: Expected shapes of s-dependences of $\frac{d^2\sigma}{d\xi dt}$ at fixed t and ξ for the four different combinations of possibilities, with and without an s-dependent K, and with and without the second term in $\sigma^{total}_{\mathcal{P}p}$. Although the curves are calculated at $-t = 1$ GeV^2 using the results of Fit "A" (see Table 7), their essential properties are the same at all t values.
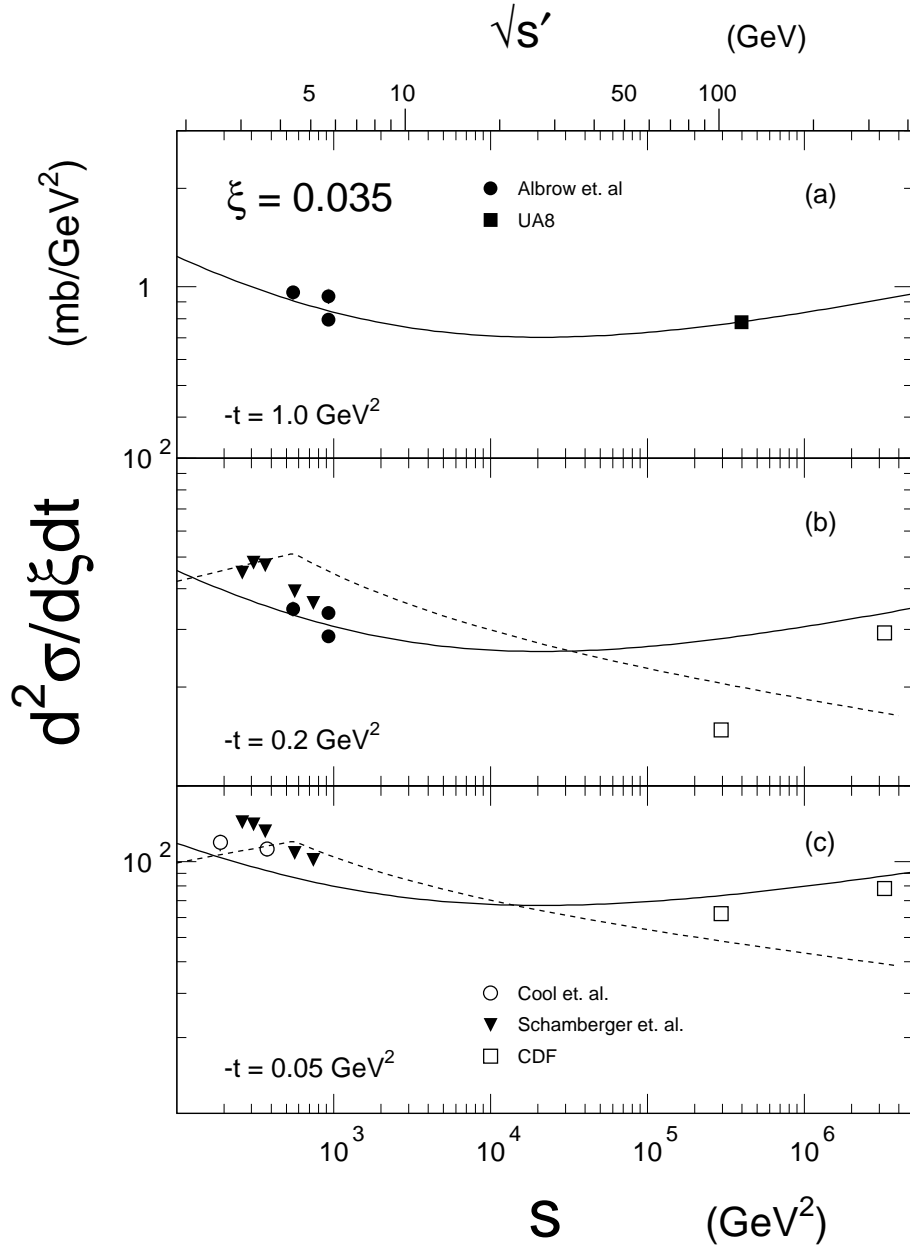
Figure 26: $\frac{d^2\sigma}{d\xi dt}$ vs. s at fixed $\xi = 0.035$ and at three different t-values. The solid curves are calculated from Fit "A" in Table 7. The dashed curves are calculated using the renormalized flux factor of Ref. [29]. The references are: Albrow et al.[15], Schamberger et al.[25], Cool et al.[26] and the CDF Collaboration[28]. See the discussion of the CDF points in the text.
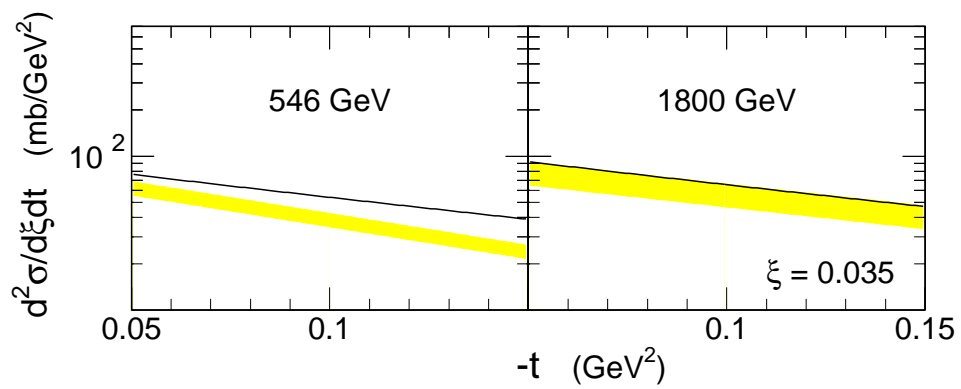
Figure 27: Bands are the CDF differential cross sections calculated at $\xi = 0.035$ from their fitted functions; widths are $\pm 1\sigma$ error on the amplitudes (as explained in the text, "signal" and "background" are added together). The curves are from the same calculations used for the solid curves in Fig. 26.
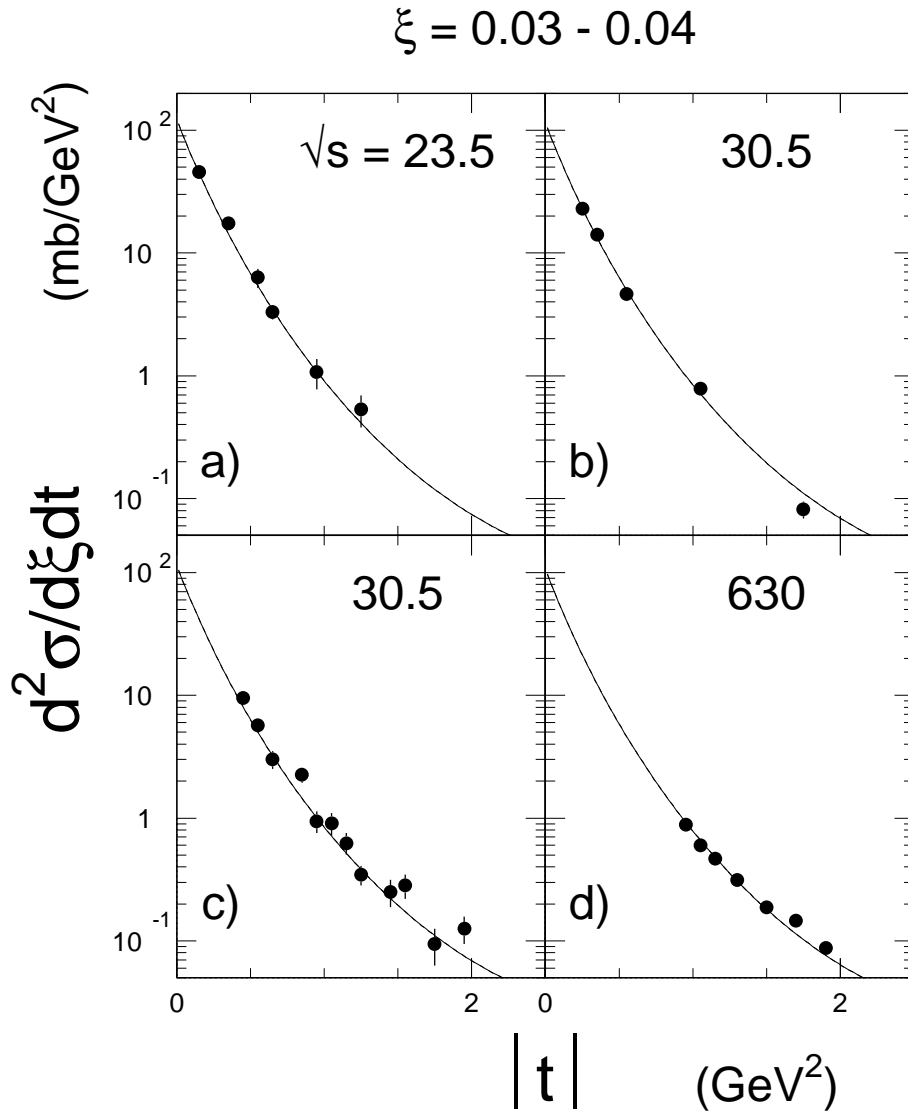
Figure 28: Differential cross section, $\frac{d^2\sigma}{d\xi dt}$, vs. $|t|$, for 3 ISR measurements[15] and UA8. Where more than one data point exists in the ξ interval, 0.03–0.04, their average is shown on this plot; thus, 30 points are shown, although 48 were used in performing Fit "A". The curves correspond to Fit "A" in Table 7 evaluated at $\xi = 0.035$.

57
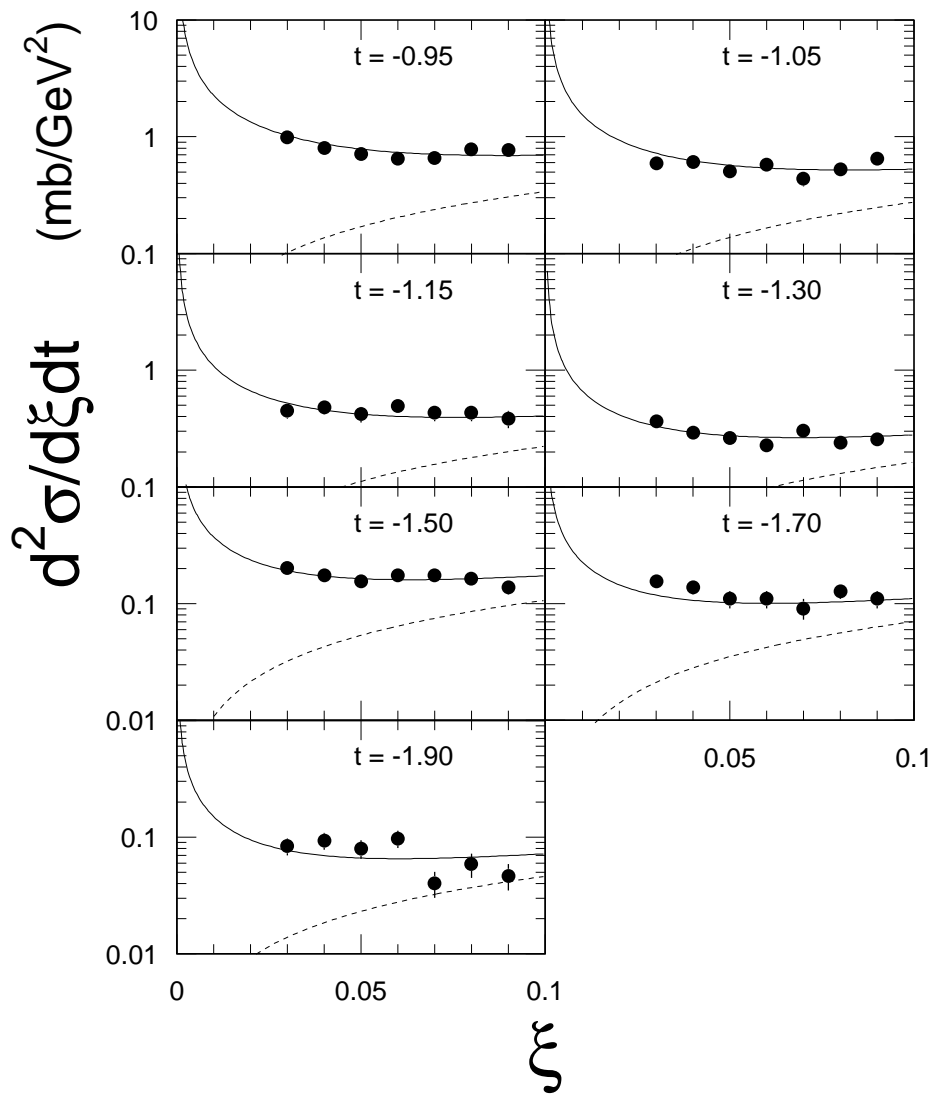
Figure 29: $\frac{d^2\sigma}{d\xi dt}$ vs. ξ for the indicated seven bins of t (given in units of GeV^2). In each case, the solid curve is the fitted function given by the sum of Eqs. 4 and 11 using Fit "D". The same fits are shown in Figs. 30. The solid curves include the non-$\mathcal{P}$omeron-exchange background from the fits. The dashed curves are the background alone.
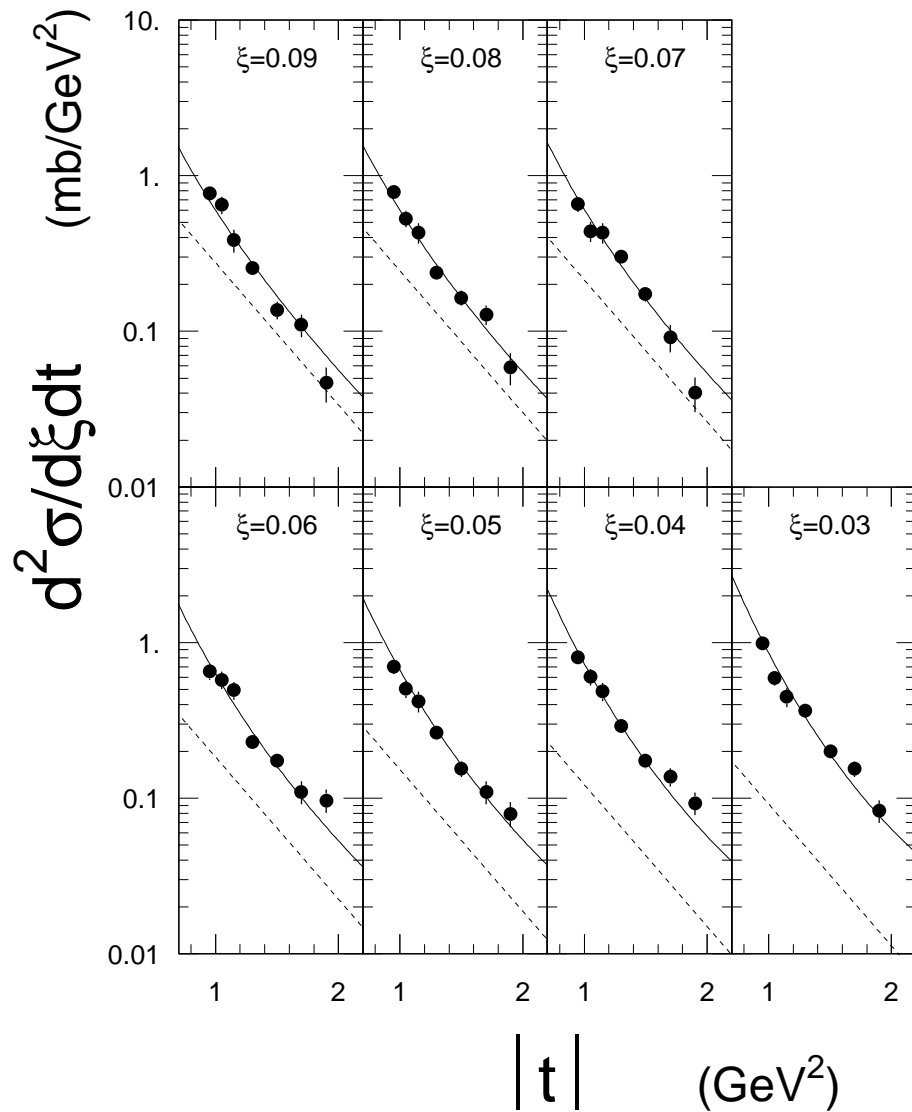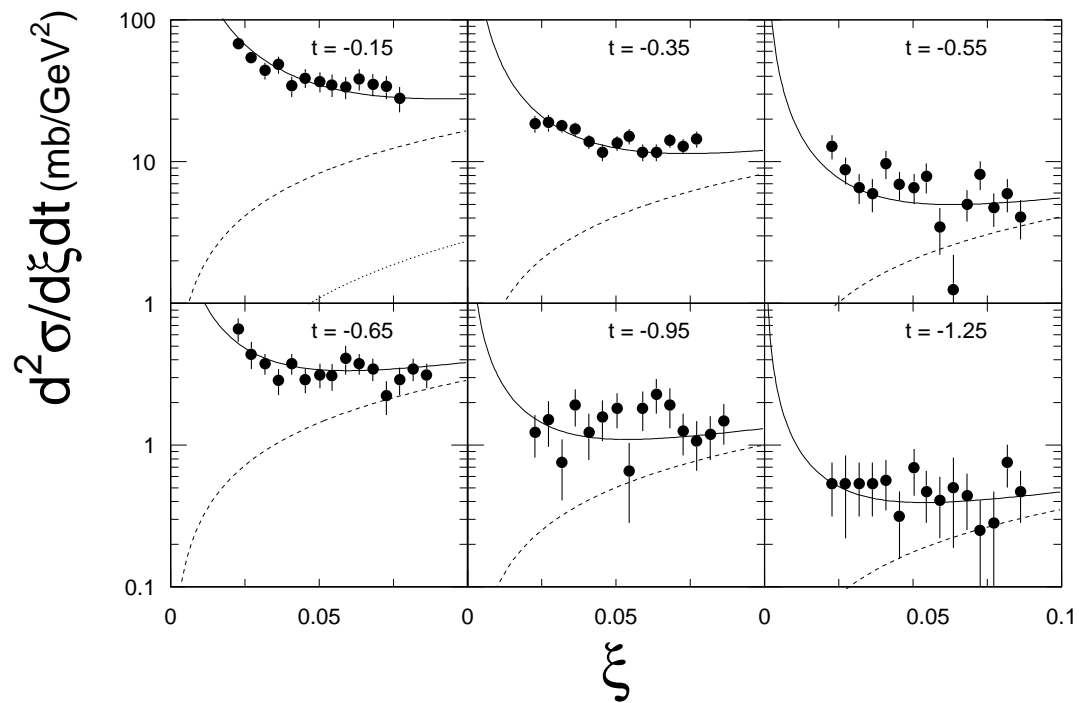
Figure 30: $\frac{d^2\sigma}{d\xi dt}$ vs. t for the indicated seven bins of ξ. In each case, the solid curve is the fitted function given by the sum of Eqs. 4 and 11 using Fit "D". The same fits are shown in Figs. 29. The solid curves include the non-$\mathcal{P}$omeron-exchange background from the fits. The dashed curves are the background alone.
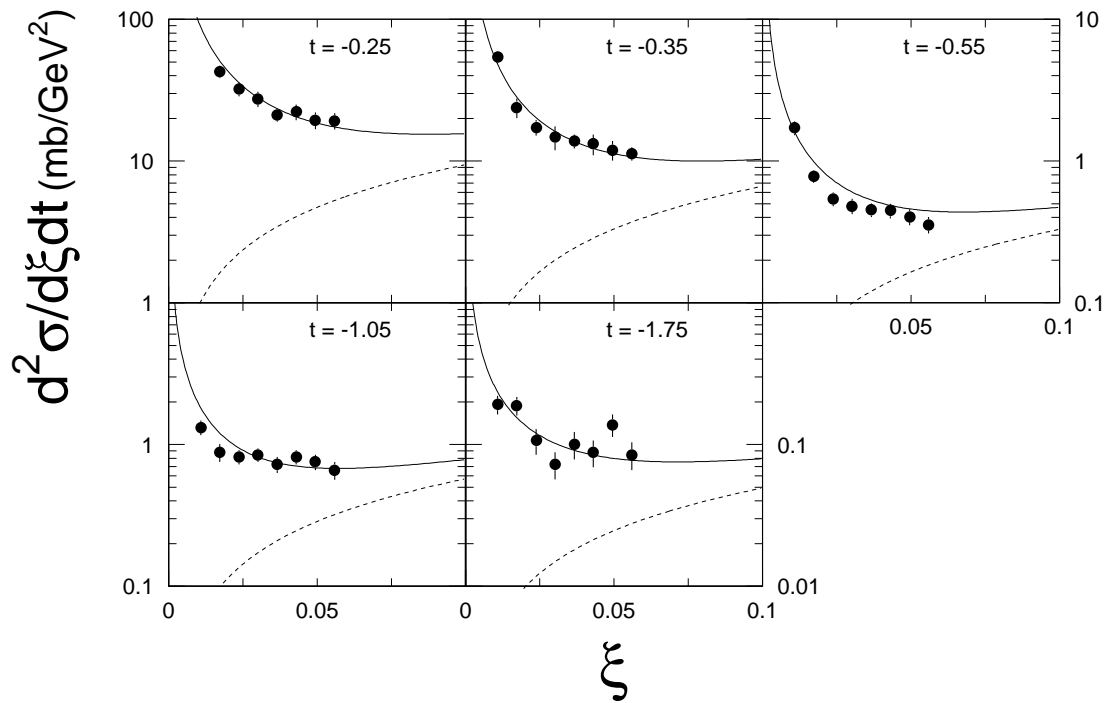
Figure 31: ISR data with $s = 551\ \mathrm{GeV}^2$[15]. In each case, the solid curve is the fitted function given by the sum of Eqs. 4 and 11 using Fit "D". Only points with $\xi > 0.03$ are used in the fit. The solid curves include the non-$\mathcal{P}$omeron-exchange background from the fits. The dashed curves are the background alone. The dotted curve on the $-t = 0.15\ \mathrm{GeV}^2$ plot is the one-pion-exchange contribution to the non-$\mathcal{P}$omeron-exchange background described in the text (not included in the fit).

Figure 32: ISR data with $s = 930$ GeV^2[15]. In each case, the solid curve is the fitted function given by the sum of Eqs. 4 and 11 using Fit "D". Only points with $\xi > 0.03$ are used in the fit. The solid curves include the non-$\mathcal{P}$omeron-exchange background from the fits. The dashed curves are the background alone.
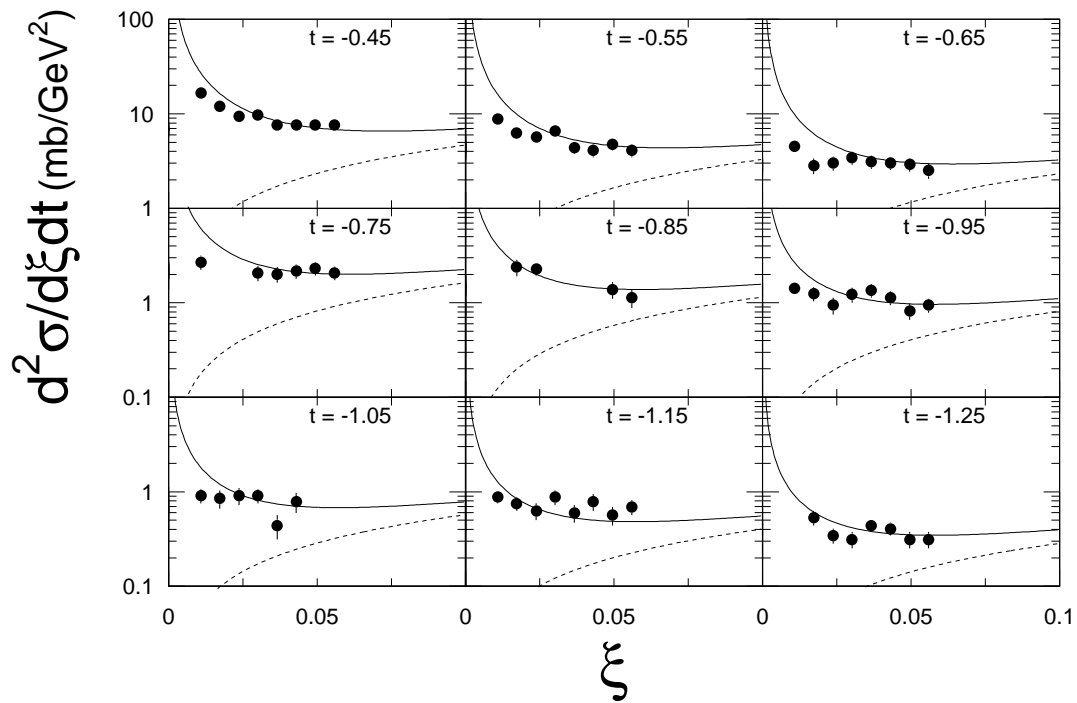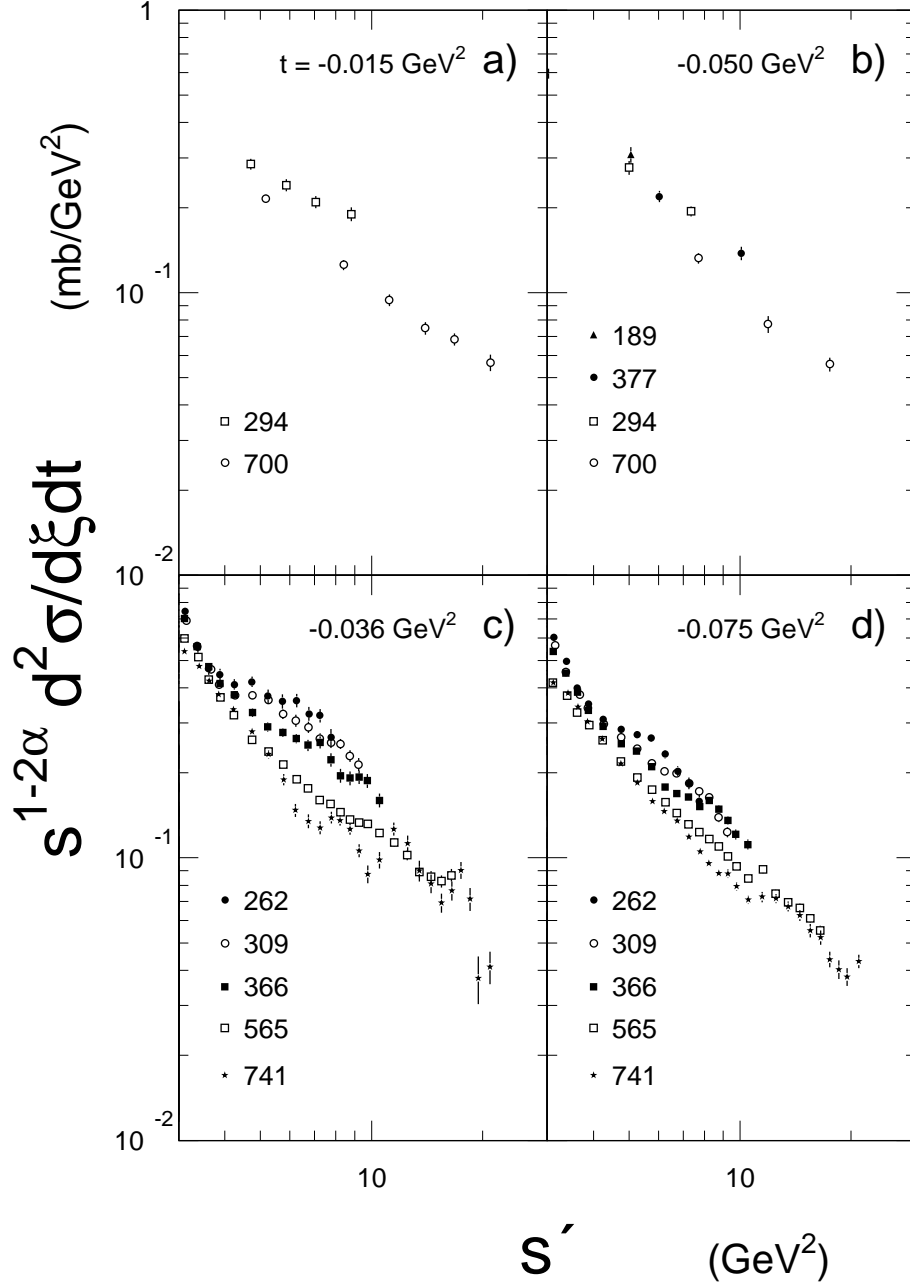
Figure 33: A second set of ISR data with $s = 930$ GeV^2[15]. In each case, the solid curve is the fitted function given by the sum of Eqs. 4 and 11 using Fit "D". Only points with $\xi > 0.03$ are used in the fit. The solid curves include the non-$\mathcal{P}$omeron-exchange background from the fits. The dashed curves are the background alone.

Figure 34: The quantity, $s^{1-2\alpha(t)} \cdot \frac{d^2\sigma}{d\xi dt}$ vs. s' at four values of t. The s values (in GeV^2) are shown in each case. References are: (a,b)[26, 27]; (c,d)[25]. Smaller s'-values are not shown in order to avoid distortions due to resolution. In order to minimize non-$\mathcal{P}$omeron-exchange background, only points with $\xi < 0.03$ are plotted.
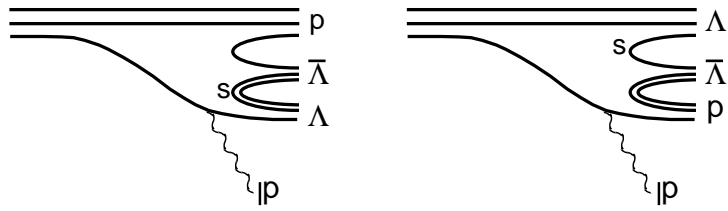
Figure 35: The diagrams show the dominant $\mathcal{P}$omeron-proton interaction processes for React. 14 which correspond to the two peaks seen in Refs. [52, 53].
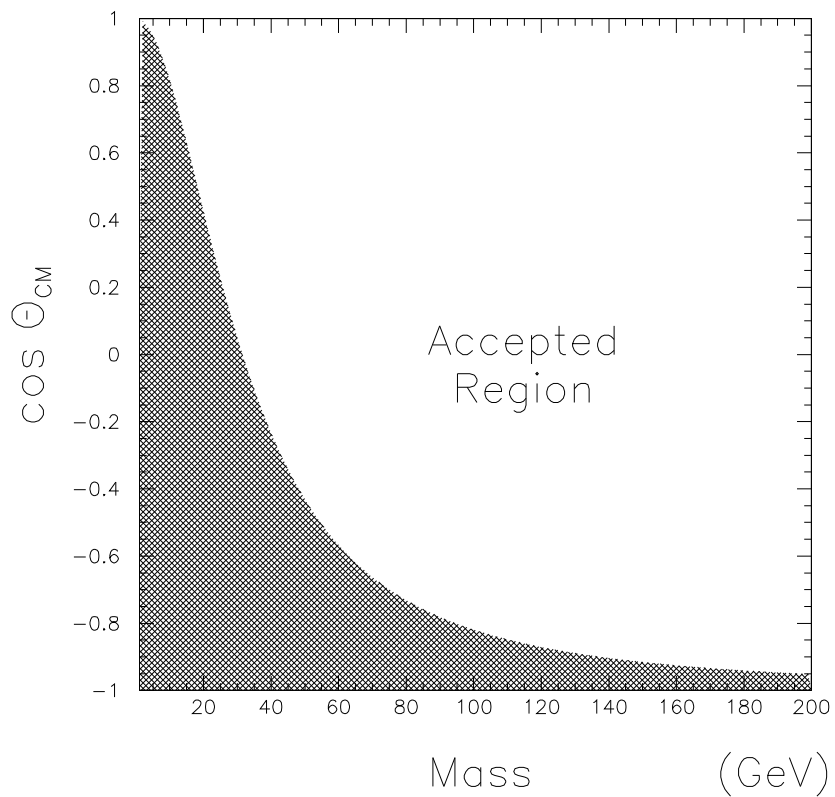
Figure 36: $cos(\theta_{CM})$ acceptance range in the UA2 calorimeter as a function of the mass of the diffractive system. The unshaded region shows the range which is accepted. The asymmetry in acceptance is due to the motion of the diffractive center-of-mass in the laboratory. $cos(\theta_{CM}) > 0$ is the $\mathcal{P}$omeron hemisphere.
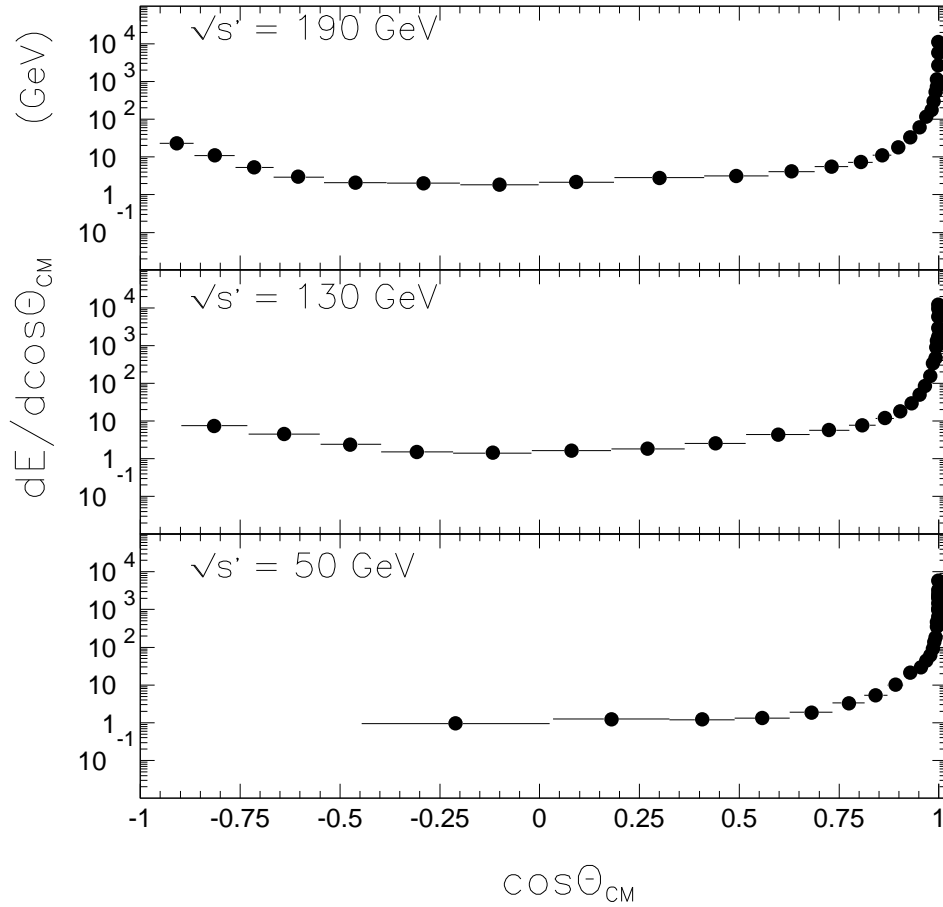
Figure 37: Average energy flow per event in the diffractive center-of-mass for three mass bins. Each point corresponds to the set of UA2 calorimeter cells with a common θ_{LAB}. In constructing the plot, the energy, and $\cos(\theta_{\mathrm{LAB}})$ from each set of cells, are transformed into the diffractive center-of-mass. On each plot, $\cos(\theta_{CM}) > 1$ corresponds to the $\mathcal{P}$omeron hemisphere. The striking peaks at $\cos(\theta_{CM}) = \pm 1$ are characteristic of a p_t-limited longitudinal event structure.